Titre: Title:	Multi-scale modeling of distortion in the non-flat 3D woven composite part manufactured using resin transfer molding
Auteurs: Authors:	Anton Trofimov, Jeremy Le-Pavic, Christophe Ravey, William Albouy, Daniel Therriault, & Martin Lévesque
Date:	2021
Type:	Article de revue / Article
Référence: Citation:	Trofimov, A., Le-Pavic, J., Ravey, C., Albouy, W., Therriault, D., & Lévesque, M. (2021). Multi-scale modeling of distortion in the non-flat 3D woven composite part manufactured using resin transfer molding. Composites Part A: Applied Science and Manufacturing, 140, 106145 (19 pages). https://doi.org/10.1016/j.compositesa.2020.106145

Document en libre accès dans PolyPublie
Open Access document in PolyPublie

URL de PolyPublie: PolyPublie URL:	https://publications.polymtl.ca/10429/
Version:	Version finale avant publication / Accepted version Révisé par les pairs / Refereed
Conditions d'utilisation: Terms of Use:	CC BY-NC-ND

Document publié chez l'éditeur officiel
Document issued by the official publisher

Titre de la revue: Journal Title:	Composites Part A: Applied Science and Manufacturing (vol. 140)
Maison d'édition: Publisher:	Elsevier
URL officiel: Official URL:	https://doi.org/10.1016/j.compositesa.2020.106145
Mention légale: Legal notice:	© 2021. This is the author's version of an article that appeared in Composites Part A: Applied Science and Manufacturing (vol. 140) . The final published version is available at https://doi.org/10.1016/j.compositesa.2020.106145. This manuscript version is made available under the CC-BY-NC-ND 4.0 license https://creativecommons.org/licenses/by-nc-nd/4.0/

Multi-scale modeling of distortion in the non-flat 3D woven composite part manufactured using Resin Transfer Molding

Anton Trofimov[a], Jeremy Le-Pavic[b], Christophe Ravey[b], William Albouy[b], Daniel Therriault[a], Martin Lévesque[a,]

[a] *Laboratory for Multiscale Mechanics, Polytechnique Montréal, Montréal, QC H3C3A7, Canada*
[b] *Safran Composites, a technology platform of Safran Tech, Itteville, 91760, France*

Abstract

This paper presents a multi-scale thermo-chemo-mechanical simulation predicting the distortion of a 3D woven composite part manufactured using the Resin Transfer Molding (RTM) process. The multi-scale numerical procedure relied on an anisotropic temperature- and degree of cure-dependent viscoelastic constitutive law whose parameters were obtained from experimental data and a blackbox optimization algorithm. Analytical (at the micro-scale) and numerical (at the meso-scale) homogenization procedures were used to compute the effective coefficients of thermal expansion and chemical shrinkage. An actual 3D woven non-flat composite specimen exhibiting variations in properties and thickness was designed and manufactured using the RTM process. The contoured geometry of the manufactured part was digitized using an industrial optical 3D scanner and compared against the developed multi-scale numerical predictions. It was found that the presented approach was capable of qualitative and, in some cases, quantitative prediction with the highest accuracy $\sim 2.8\%$ of manufacturing induced geometrical distortions.

Keywords: viscoelasticity, multi-scale modeling, homogenization, 3D woven composite, resin transfer molding

List of Symbols

ε^{mech}	Viscoelastic second order strain tensor	α	Degree of cure
$\varepsilon^{non-mech}$	Stress free second order strain tensor	t	Time
$\varepsilon_{CCS}^{non-mech}$	Stress free second order strain tensor associated to the chemical shrinkage	m	Material parameter (Kamal and Sourour model)
		k_1	Chemical reaction rate constant (Kamal and Sourour model)
$\varepsilon_{CTE}^{non-mech}$	Stress free second order strain tensor associated to the thermal expansion	k_2	Chemical reaction rate constant (Kamal and Sourour model)
		T	Temperature

---

*Corresponding author
   Email address:* `martin.levesque@polymtl.ca` (Martin Lévesque)

R	Universal gas constant		λ	DiBenedetto material parameter
A_i	Arrhenius constant (Kamal and Sourour model)		$\boldsymbol{\chi}$	Hidden (internal) variables
E_i	Activation energy (Kamal and Sourour model)		$T_g^{(\infty)}$	Fully cured resin's glass transition temperature
$\mathbf{C}^{(\infty)}$	Fully relaxed fourth order stiffness tensor		$\boldsymbol{\varepsilon}^T$	Chemical shrinkage second order strain tensor
τ_k	Relaxation time		$\boldsymbol{\varepsilon}^C$	Thermal expansion second order strain tensor
N	Number of relaxation times		$\boldsymbol{\theta}$	Coefficient of thermal expansion second order tensor
$\mathbf{p}(\alpha)$	Adjustable fourth order tensor for cure-dependency		$\boldsymbol{\beta}$	Coefficient of chemical shrinkage second order tensor
a_T	Shift factors		r_a	Cost function
$\mathbf{K}_1$	Adjustable fourth order tensor ($\mathbf{p}(\alpha)$)		$\boldsymbol{\sigma}$	Second order stress tensor
$\mathbf{K}_2$	Adjustable fourth order tensor ($\mathbf{p}(\alpha)$)		$\boldsymbol{s}$	Measured or predicted second order stress tensor (cost function equation)
$\mathbf{B}$	$6N \times 6N$ identity matrix			
$\mathbf{C}^{(k)}$	Adjustable fourth order relaxation tensors		M	Total number of discrete times
T_g	Glass transition temperature		F	Total number of elements
E_{a1}	Activation energy below T_g (Arrhenius equation)		g	Loadcase number
E_{a2}	Activation energy above T_g (Arrhenius equation)		V	Volume
			$V^{(l)}$	Volume of the element
a_1	Adjustable model parameter (Arrhenius equation)		ϕ	Inhomogeneities volume fraction
a_2	Adjustable model parameter (Arrhenius equation)		$\mathbf{N}$	Stiffness contribution fourth order tensor (Mori-Tanaka scheme)
b_1	Adjustable model parameter (Arrhenius equation)		G	Shear modulus
T_g^0	Uncured resin's glass transition temperature		λ	Lamé's first parameter
			$\mathbf{S}$	Compliance fourth order tensor
			u_i	Displacements

1. Introduction

Resin Transfer Molding (RTM) comprises in injecting a viscous thermoset resin into a dry fibrous preform and subsequently curing it until full consolidation. The process involves significant temperature variations that trigger the development of residual stresses leading to matrix cracking, delamination and/or part distortion [1, 2, 3]. Residual stresses and distortions result mainly from the dissimilar fibers and matrix coefficients of thermal expansion, the polymer cure shrinkage and tool-part interaction [4, 5, 6, 7]. Moreover, the polymer resin evolves from a purely viscous to a viscoelastic and, ultimately, to an elastic mechanical behavior throughout the process [8, 9].

The structure of a 3D woven composite is hierarchical. At the meso-scale, the structure is made of tows that are classified as warp (longitudinal) and weft (transverse), and of a polymer matrix. At the micro-scale, the tows are assumed to be made of carbon fibers and the polymer matrix. All of these features interact with each other and influence the overall part performance. Therefore, the prediction of the macro-scale warpage during manufacturing requires a robust constitutive model for the polymer matrix and an efficient multi-scale procedure [10, 11].

A number of constitutive models accounting for the different thermo-chemo-mechanical phenomena active during manufacturing have been developed to predict composites part distortion. Authors in [12] used temperature dependent elastic properties to predict the spring-in angle of a U-shaped laminate. Johnston proposed the so-called Cure Hardening Instantaneous Linear Elastic (CHILE) model to represent the resin's stiffness evolution with the degree of cure and temperature [13]. The CHILE model was used by several research groups to predict the geometrical distortion built up during the process [3, 14]. Recently, Wang et.al [15] used a multi-scale approach based on the CHILE model to predict the process-induced residual strains in the RTM composite. However, the CHILE model neglects the viscoelastic nature of the polymer matrix and the stress relaxation occurring during the process. A degree of cure- and temperature-dependent viscoelastic model has been developed for epoxy resins below their glass transition temperature (T_g) [16]. This model was extended to an orthotropic 3D woven composite and used to predict creep strains below the resin's T_g [17]. A detailed comparison of distortion predictions during post curing using different elastic and viscoelastic models was performed in [18, 19, 20]. It was shown that the main source of warpage in 3D interlock composite parts was related to creep strains. Therefore, a degree of cure- and temperature-dependent viscoelastic model is needed to accurately predict the final part distortion. Such a complex viscoelastic model requires extensive polymer matrix characterization.

Numerical multi-scale homogenization is usually used to compute macroscopic properties by spatially averaging stresses and strains fields at the micro- and meso-scales. The technique is computationally expensive as it requires explicit representations of the microstructure by relying on the concept of Representative Volume Element (RVE) and computation of the local stress and strain fields in the RVE when external loads are applied. The technique has been applied to elastic [21, 22, 23], viscoelastic [24, 25, 26], thermoviscoelastic [27, 28, 29], temperature and degree-of-cure dependent materials [30, 16]. RVEs can be an 'artificial' statistically representative microstructures [31, 32, 33, 34] or 'real' representations generated from material images taken by Computed Microtomography (μCT) [35, 36, 37].

This paper presents a novel multi-scale thermo-chemo-mechanical procedure to predict distortion in a 3D woven composite part using a temperature- and degree-of-cure dependent viscoelastic constitutive model. The procedure provides a unique versatile framework capable of simulating the anisotropic behavior of 3D woven composites whose physical state evolves over the RTM manufacturing process. Since the RTM allows the design and manufacturing of composites featuring complex geometries and weaving architectures, we experimentally validated distortion predictions

on a non-flat 3D woven carbon fiber reinforced epoxy composite part with a non-uniform fabric orientation.

The paper is organized as follows: Section 2 recalls background information on temperature- and degree-of-cure dependent constitutive models. This section provides the essential information to follow this paper and to show the novelty of our work with respect to existing models. The RTM of a non-flat composite part and the digitization of its geometrical contours are described in Section 3. Section 4 details the multi-scale methodology to simulate the whole RTM process. The components of stiffness, coefficients of thermal expansion and chemical shrinkage tensors at each stage of the procedure are presented in Section 5. The distortion predictions are compared to experimental data in Section 6. Discussion and final conclusions are given in Sections 7 and 8, respectively.

The modified Voigt notation has been adopted throughout the paper. Symmetric second-order tensors are expressed as six component vectors and symmetric fourth-order tensors are expressed as 6×6 matrices. Scalar quantities are denoted by light-faced letters (i.e., a, α and A), second order tensors are represented by boldfaced lowercase Greek letters (i.e., $\boldsymbol{\sigma}$), while fourth-order tensors are represented by boldfaced capital Roman letters (i.e., $\mathbf{C}$).

Note that all the values of the stiffness tensors and the expansion coefficients are normalized by the stiffness tensor component C_{11} and by the expansion coefficients at room temperature of the fully cured polymer, respectively.

2. Background information

Geometrical distortion in RTM composite parts is essentially triggered by the residual stresses build-up during manufacturing Generally, the process can be divided into two main stages: before and after demolding. Before demolding, the plate is in the mold and constrained (zero displacements), as well as submitted to a specific temperature profile. As a result, internal stresses develop and evolve with the degree of cure due to the matrix coefficient of chemical shrinkage (CCS) and evolve with the temperature variation due to the coefficient of thermal expansion (CTE). After demolding, the plate is released and cooled down to room temperature, which leads to a decrease of internal stresses and mechanical strains that develop final geometrical instabilities.

Loos et al. [38] and Svanberg et al. [39] developed a sequentially modular approach to simulate the thermo-chemo-mechanical phenomena involved in the RTM process. The degree of cure distribution as a function of time was first predicted throughout a plate with the chemical model recalled in Section 2.1. The obtained distribution, along with a known uniform temperature profile as a function of time, were input as solution-independent conditions into a time-temperature- and cure-dependent constitutive model to compute the total strain response $\boldsymbol{\varepsilon}^{tot}$ of a 3D woven composite as [19, 20]:

$$\boldsymbol{\varepsilon}^{tot} = \boldsymbol{\varepsilon}^{mech} + \boldsymbol{\varepsilon}^{non-mech}, \tag{1}$$

where $\boldsymbol{\varepsilon}^{mech}$ are viscoelastic strains and $\boldsymbol{\varepsilon}^{non-mech} = \boldsymbol{\varepsilon}^{non-mech}_{CCS} + \boldsymbol{\varepsilon}^{non-mech}_{CTE}$, where $\boldsymbol{\varepsilon}^{non-mech}_{CCS}$ and $\boldsymbol{\varepsilon}^{non-mech}_{CTE}$ are the stress free strains associated to the chemical shrinkage and thermal expansion, respectively. Courtois et al. [17] have developed a three-dimensional constitutive model and proposed a multi-scale procedure to identify its parameters. The details on the work of Courtois et al. are given in Section 2.2.1.

2.1. Resin cure kinetics

The resin cure kinetics was modeled with Kamal and Sourour phenomenological model as [40]

$$\frac{d\alpha}{dt} = (k_1 + k_2\alpha^m)(1 - \alpha^n), \tag{2}$$

where t is the time, α is the degree of cure, m is a material constant and k_1 and k_2 are the chemical reaction rate constants described by Arrhenius', equation as

$$k_i = A_i \exp\left(\frac{-E_i}{RT}\right), \tag{3}$$

where T is the temperature, R, A_i and E_i are the universal gas constant, the Arrhenius constant and activation energy, respectively. Differential Scanning Calorimetry (DSC) tests were performed on the polymer resin studied in this work at different heating rates and the model parameters were adjusted until they best fitted the experimental data (see [16] for details).

2.2. Mechanical model

2.2.1. Mechanical strains

Courtois et al. [17] have developed a general and three-dimensional temperature- and degree of cure viscoelastic constitutive model within the framework of the thermodynamics of irreversible processes [41, 42, 43]. The model can be used for both the polymer matrix and the composite. This model reads:

$$\boldsymbol{\sigma}(t) = \mathbf{C}^{(\infty)} : \boldsymbol{\varepsilon} + \int_0^t \sum_{k=1}^N \mathbf{p}(\alpha) \odot \mathbf{C}^{(k)} \exp\left[-\frac{1}{\tau_k}\left(\int_0^t \frac{1}{a_T(T,\alpha)}d\rho \right.\right.$$
$$\left.\left. - \int_0^\tau \frac{1}{a_T(T,\alpha)}d\rho\right)\right] : \frac{d\boldsymbol{\varepsilon}}{d\tau}dt, \tag{4}$$

where $\mathbf{C}^{(\infty)}$ is the fully relaxed tensor, N is the number of relaxation times, $\odot$ is Hadamard product [44], $\mathbf{p}(\alpha) = \mathbf{K}_1\alpha + \mathbf{K}_2$ is a fourth order symmetric and positive definite tensor that introduces anisotropic cure-dependency, where $\mathbf{K}_1$ and $\mathbf{K}_2$ are adjustable fourth order tensors. The $\mathbf{C}^{(k)}$ are fourth order positive semi-definite and symmetric adjustable relaxation tensors associated with the relaxation times τ_k. The shift factors $a_T(T,\alpha)$ in Equation (4) are expressed by an Arrhenius relationship as:

$$\log a_T = \begin{cases} \frac{E_{a1}(\alpha)}{\ln 10R}\left(\frac{1}{T} - \frac{1}{T_g(\alpha)}\right) & T < T_g(\alpha) \\ \frac{E_{a2}(\alpha)}{\ln 10R}\left(\frac{1}{T} - \frac{1}{T_g(\alpha)}\right) & T \geq T_g(\alpha), \end{cases} \tag{5}$$

where $E_{a1} = a_1 + \alpha b_1$ and $E_{a2} = a_2 + \alpha b_2$ are activation energies below and above the glass transition temperature $T_g(\alpha)$ and a_1, b_1, a_2 and b_2 are adjustable scalar parameters. $T_g(\alpha)$ was obtained from the DiBenedetto equation as

$$\frac{T_g(\alpha) - T_g^{(0)}}{T_g^{(\infty)} - T_g^{(0)}} = \frac{\lambda\alpha}{1 - (1 - \lambda)\alpha}, \tag{6}$$

where T_g^0 and $T_g^{(\infty)}$ are the uncured ($\alpha = 0$) and fully cured ($\alpha = 1$) resin's glass transition temperatures, respectively, and λ is a material constant.

The constitutive relationship (4) is the solution to the differential equation [45]:

$$\boldsymbol{\sigma}(t) = \mathbf{L}^{(1)} : \boldsymbol{\varepsilon}(t) + \mathbf{p}(\alpha) \odot \mathbf{L}^{(2)} : \boldsymbol{\chi}(t) \tag{7a}$$

$$a_T \mathbf{B} : \dot{\boldsymbol{\chi}} + \mathbf{L}^{(3)} : \boldsymbol{\chi} + \mathbf{p}(\alpha) \odot \left(\mathbf{L}^{(2)}\right)^T : \boldsymbol{\varepsilon} = \mathbf{0}, \tag{7b}$$

where $\boldsymbol{\chi}$ are so-called hidden variables, $\dot{\boldsymbol{\chi}}$ are their time derivatives, $\mathbf{B}$ is the $6N \times 6N$ identity matrix, where N is the number of relaxation times, $\mathbf{L}^{(1)}$ and $\mathbf{L}^{(3)}$ are symmetric positive definite tensors that can be expressed as:

$$\mathbf{L}_1 = \mathbf{C}^{(\infty)} + \mathbf{p}(\alpha) \odot \sum_{k=1}^{N} \mathbf{C}^{(k)} \tag{8a}$$

$$\mathbf{L}_3 = \left[\frac{1}{\tau_k}\mathbf{B}\right]. \tag{8b}$$

$\mathbf{L}_2$ is a tensor composed of triangular tensors $\mathbf{L}_2 = \left(\mathbf{L}_2^{(1)}|\mathbf{L}_2^{(2)}|...|\mathbf{L}_2^{(N)}\right)$ obtained by the Cholesky decomposition of $\frac{1}{\tau_k}\mathbf{C}^{(k)}$ so that:

$$\mathbf{L}_2^{(k)} : \left(\mathbf{L}_2^{(k)}\right)^T = \frac{1}{\tau_k}\mathbf{C}^{(k)}. \tag{9}$$

Equations (7)(a,b) were implemented for numerical analysis using the Backward – Euler Finite Differences scheme as [46]:

$$\boldsymbol{\chi}^{n+1} = \boldsymbol{\chi}^n + \Delta t \dot{\boldsymbol{\chi}}^{n+1} = \mathbf{W}_1 : \boldsymbol{\chi}^n + \mathbf{W}_2 : \boldsymbol{\varepsilon}^{n+1}, \tag{10}$$

where $\mathbf{W}_1 = \left(\mathbf{B} + \Delta t \mathbf{A} : \mathbf{L}_3\right)^{-1}, \mathbf{W}_2 = -\Delta t \mathbf{W}_1 : \mathbf{A} : \mathbf{p}(\alpha) \odot \left(\mathbf{L}_2\right)^T, \mathbf{A} = \frac{\mathbf{B}}{a_T(T,\alpha)}$. The required stress at the $n+1$ step becomes:

$$\boldsymbol{\sigma}^{n+1} = \mathbf{L}_1 : \boldsymbol{\varepsilon}^{n+1} + \mathbf{p}(\alpha) \odot \mathbf{L}_2 : \boldsymbol{\chi}^{n+1}. \tag{11}$$

Implementing Equations (10) and (11) requires the following parameters: i) the T_g^0 and $T_g^{(\infty)}$, as well as λ in DiBenedetto's equation (6); ii) the adjustable scalars a_1, b_1, a_2 and b_2 of Arrhenius' relationship (5); iii) the fourth order tensors $\mathbf{C}^{(\infty)}$, $\mathbf{C}^{(k)}$, $\mathbf{K}_1$ and $\mathbf{K}_2$ of the temperature- and cure-dependent viscoelastic constitutive model of Equation (4).

In the work of Courtois et al. [17], the multi-scale identification procedure of a constitutive model parameters started with the prediction of a neat polymer model parameters from the DSC and DMA (Dynamic Mechanical Analysis) experiments that were conducted by Courtois et al. in [16].

Courtois et al. extracted the T_g^0 and $T_g^{(\infty)}$ from the DSC test data and the material parameter λ was obtained by fitting DSC measurements with DiBenedetto's equation (6).

The DMA tests were performed by Courtois et al. with a three-point bending clamp in a TA Instruments Q800 DMA apparatus for a strain level of $\varepsilon^0 = 0.1\%$, at temperatures ranging from 30°C to 150°C and for degrees of cure $\alpha = 1, 0.9, 0.85, 0.8$. It should be noted that Courtois et al. verified that the polymer behaved as a linearly viscoelastic material under these conditions and that the maximum test temperature was adjusted to avoid degree of cure evolution in partially cured specimens. Starting from 30°C, the specimens were bent to 0.1% of strain and held at a constant load for 90 minutes to measure relaxation behavior. Next, the load was removed to allow 10 minutes

of recovery. The temperature was then ramped at 1.5° C/min in 10 minutes and stabilized at the new level for an additional 5 minutes. This procedure was repeated up to a temperature below the T_g (150° for the fully cured specimen for example).

The relaxed modulus $\mathbf{C}^{(\infty)}$ was taken as the stabilized response from the fully cured samples at the highest temperature. The rest of the components were obtained by fitting experimental data with Equation (4). Note that the tensor parameters were reduced to scalars for an isotropic material, which is the assumption that was made for the polymeric matrix studied in [17]. Moreover, the matrix' Poisson's ratio was assumed as a constant.

Courtois et al.[17] used the obtained neat resin behavior to compute the tows' model parameters by fitting numerical homogenization data with Equation (4). Another homogenization procedure was carried out to obtain the mesoscopic structure homogenized behavior which was fitted again with Equation (4) to compute the final parameters of the constitutive model. Note that T_g^0, $T_g^{(\infty)}$, λ, a_1 and b_1 were set to the values obtained for the neat polymer and were not fitted during these steps.

Courtois et al. [17] used the built-in Matlab function *fminsearch* to best-fit the necessary components below the T_g minimizing the discrepancy between stress predictions and experimental or homogenized values. One of the main limitations of the function *fminsearch* is that it can provide local minima and requires fairly close initial guesses for optimization problems featuring more than 10 variables to converge [47].

The optimization procedure in the work of Courtois et al. was limited to orthotropic material symmetry when dealing with the homogenized composite properties. The three shear components of the stiffness tensors $\mathbf{C}^{(k)}$ were treated independently as three 1D problems in a first stage. Then, the remaining six independent components were simultaneously optimized to best fit the stress response of a RVE submitted to three uni-axial deformation states as a response to a three uniaxial deformations (along the global coordinates). Courtois et al.' optimization procedure cannot be directly applied to the case of general anisotropy.

Recall that, due to thermodynamics restrictions, all tensors in Equation (4) must be symmetric. Moreover, tensors $\mathbf{C}^{(k)}$ must be positive semi-definite, and tensors $\mathbf{K}_1$ and $\mathbf{K}_2$ must be positive definite. To ensure these requirements, trials generated by *fminsearch* algorithm were checked at each optimization step and disregarded if the principles were violated. As a result, the developed optimization procedure [17] promoted the local minima solution and required significant computational resources as many steps were skipped.

2.2.2. Expansional strains

Bogetti et al. [48] and Svanberg et al. [39] computed the chemical shrinkage and thermal expansion strains as:

$$\boldsymbol{\varepsilon}^T(t + \Delta t) = \boldsymbol{\varepsilon}^T(t) + \boldsymbol{\theta}(T)\Delta T \tag{12a}$$

$$\boldsymbol{\varepsilon}^C(t + \Delta t) = \boldsymbol{\varepsilon}^C(t) + \boldsymbol{\beta}(T)\Delta \alpha \tag{12b}$$

where ΔT and $\Delta \alpha$ are the temperature and degree of cure increments within the time step, and $\boldsymbol{\theta}(T)$ and $\boldsymbol{\beta}(T)$ are the tensors of effective coefficients of thermal expansion and chemical shrinkage, respectively. In the framework of multi-scale simulation, the effective coefficients need to be obtained using a procedure similar to that recalled in Section 2.2.1.

Authors measured the CTE and CCS of a polymer matrix using thermomechanical analysis (TMA) [49] and a Pressure, volume and Temperature -Heterogeneous Anisotropic Deformation and Degree Of Cure monitoring (PvT-HADDOC) device in [50]. At the micro-scale, numerical and
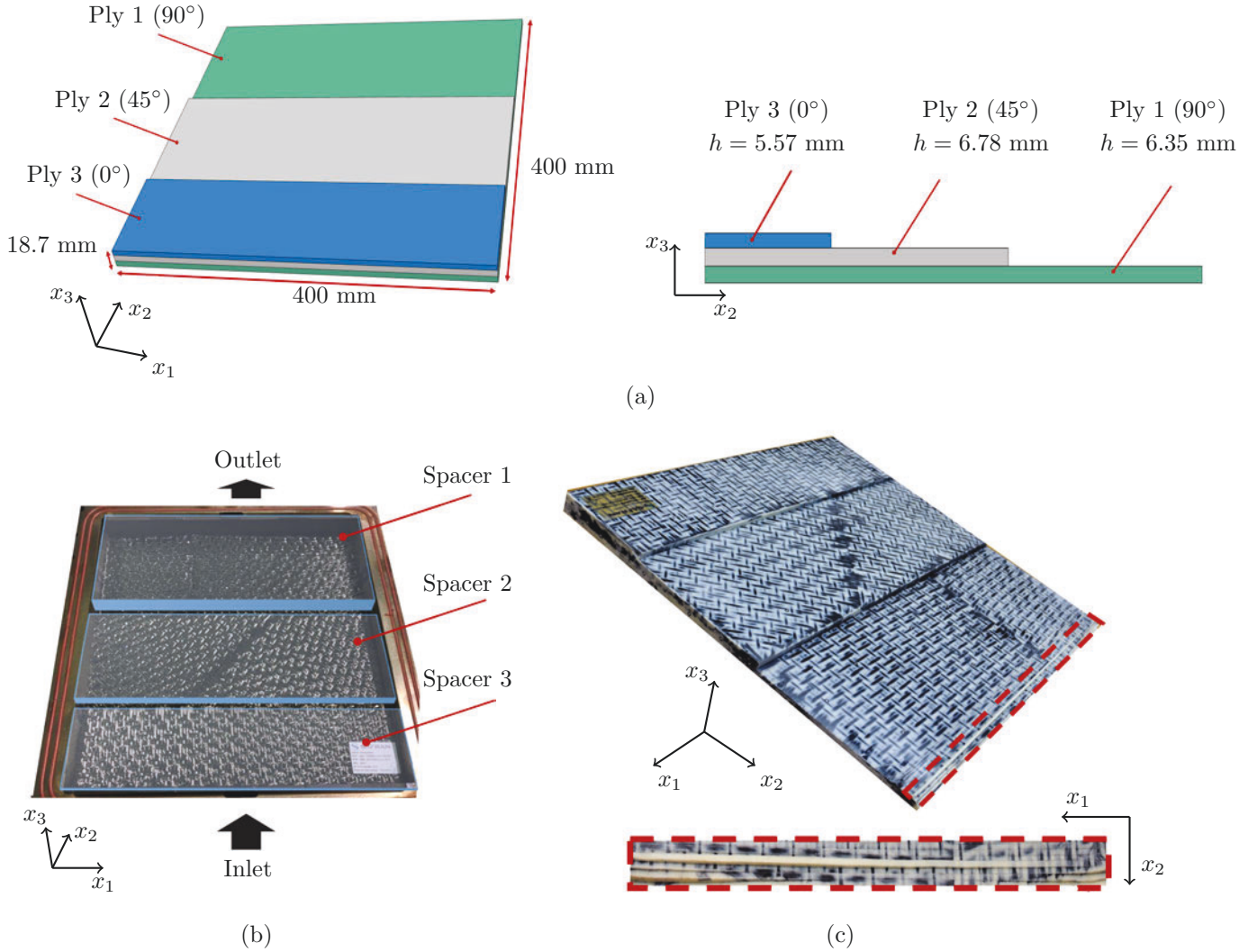
Figure 1: Manufacturing of a non-flat composite plate consisting of a 3D woven carbon fiber reinforcement and commercial DGEBF (DiGlycidyl Ether of Bisphenol F) epoxy matrix: (a) 3D CAD design of the plate and side view; (b) in-mold layup with schematic representation of spacers placement as well as the injection direction; (c) final RTM manufactured non-flat plate with a highlighted resin rich area.

analytical homogenization were used to compute CTE and CCS of the tows [51]. Khan and Muliana [52] have shown that the Mori-Tanaka scheme provides satisfactory estimation of the effective CTE of unidirectional composites with high volume fraction of fibers. At the meso-scale, analytical homogenization schemes based on a one particle approximation provided unreliable results for 3D woven composites, thus Finite Element Method (FEM) homogenization was used to predict the composite's effective properties [53, 54].

To the best of our knowledge, there is no published work combining all the required steps of a multi-scale procedure to compute the overall CTE and CCS of a 3D woven composite for simulation of the RTM process. This paper fills this gap.

3. Materials and methods

A 3D woven carbon fiber interlock preform injected by a commercial DGEBF (DiGlycidyl Ether of Bisphenol F) epoxy matrix was studied (the full specifications cannot be disclosed for
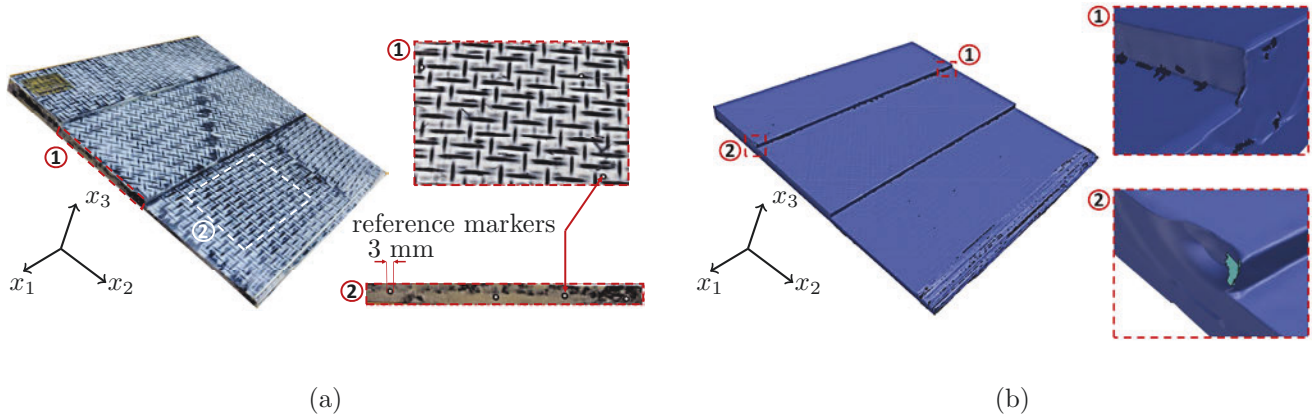
Figure 2: Digitization process for the three-ply variable thickness plate studied in this work: (a) sample with applied reference markers detailed in closeup views; (b) reconstructed surface with closeup views showing examples of poor reconstruction.

confidentiality reasons). Figure 1 schematizes the chosen goemetry. A step-wise geometry (Figure 1(a)) made of three plies oriented at 0°, 45° and 90° was chosen to test the predictive model on a specimen exhibiting variations in weaving architecture and thickness. A longitudinal injection was carried out in a rectangular RTM steel mold with an internal cavity of 400 mm × 400 mm × 32 mm and three spacers to fill gaps in the mold and ensure the designed thickness variation (Figure 1(b)).

Once the preform was draped, the mold was closed and preheated at 160°C. The epoxy system was heated above 100°C to reduce its viscosity and degassed prior to the injection. The resin was then injected with a constant flow rate. A cure cycle with two dwell phases of one hour at 160°C and two hours at 180°C was adopted to ensure complete resin curing. The part was then cooled inside the mold until its temperature reached 100°C. Finally, the part was released from the mold, led free standing and cooled by natural convection down to room temperature (23°C). The final dimensions of the plate were 400 mm × 400 mm with the thickness of plies being 6.35 mm (ply 1), 6.78 mm (ply 2) and 5.57 mm (ply 3). Figure 1(c) shows the manufactured plate with highlighted resin rich areas. Q-2000 Modulated Differential Scanning Calorimeter (M-DSC) measurements revealed that the plate was completely cured with a degree of cure of 99.7 %.

The contoured geometries of the manufactured part were digitized with the industrial optical 3D scanner ATOS Triple Scan III. The setup consisted of two 16M pixels cameras, a projector, a 3-axis motorization kit, a rotary table and a computer installed with the GOM ATOS Professional software for post processing. According to the triple scan principle, precise fringe patterns are projected onto the surface of the object and the data is recorded by two cameras using the stereo camera principle, collecting information in the ray intersections (left camera/right camera; left camera/projector and right camera/projector).

The measuring procedure began with system calibration by placing reference point markers on the specimen surface to construct a 3D volume. Additional individual measurements were transformed to create a high-precision Computer-Aided Design (CAD) model of the plate. The markers had a diameter of 3 mm. Figure 2(a) shows the selected marker locations. Overall, 67 reference markers were placed on the plate. Since the Triple Scan technology requires a reflection of the fringe projection back to the camera system, the plate was covered with talc powder to ensure proper light reflection and contrast. Once all the preparation steps were made, an operator
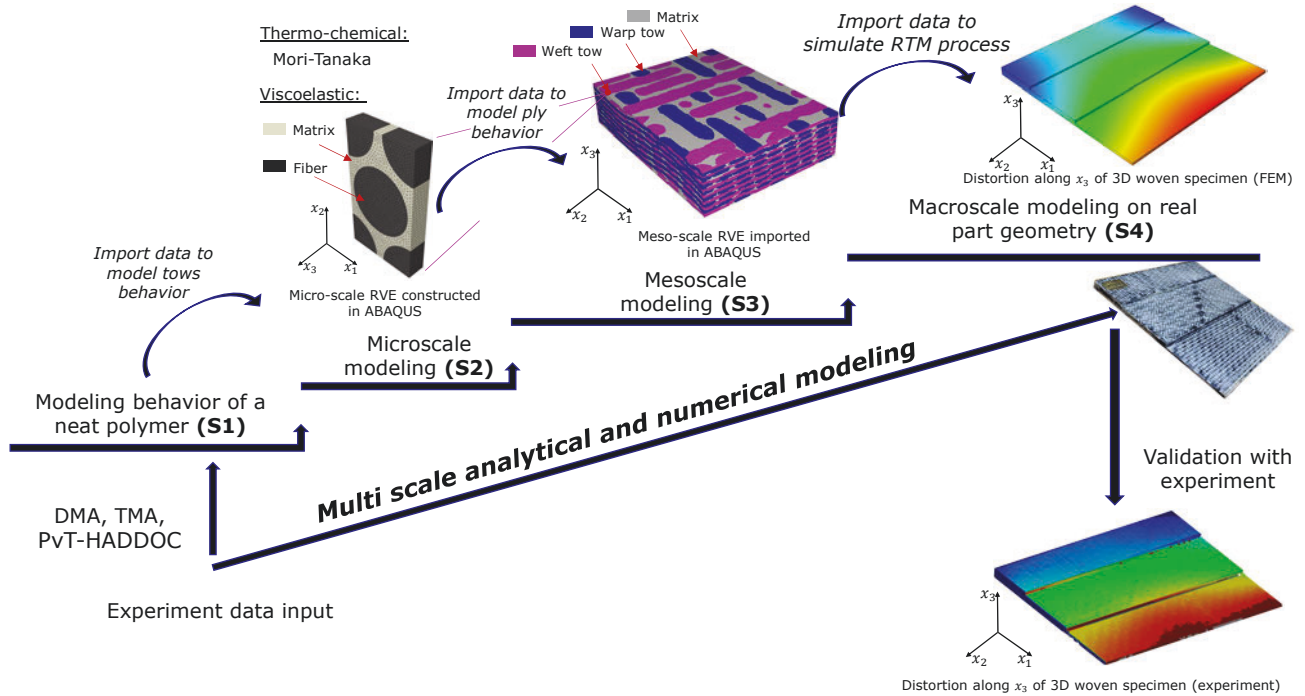
Figure 3: Multi-scale procedure to simulate the RTM process. The experimentally obtained data on the matrix' CTE, CCS and viscoelastic behavior utilizing TMA, PvT-HADDOC and DMA, respectively, is used to identify the matrix' constitutive theory parameters (S1). The obtained model is used as an input to the micro-scale homogenization procedure to identify the parameters of a constitutive model that predicts the tows effective behaviour (S2). The computed tows behavior is input into the meso-scale model to identify the constitutive theory parameters for the ply's effective behaviour (S3). The obtained ply effective behavior is used to simulate the RTM process (S4).

placed the plate on a rotary table and took a set of images (each of which contained up to 16M measurement points) in various positions and camera lenses orientations. Finally, a digital 3D model of the plate was generated using the GOM ATOS Professional software by postprocessing the images.

The reconstruction process poorly reproduced the contours of the lateral surfaces when changing from one ply to another (the steps), which can be explained by the small thicknesses of the plies containing only one marker. Figure 2(b) presents the final digitized model with highlighted areas demonstrating reconstruction artefacts. It will serve as a reference to compare experimental data against numerical predictions (Section 6).

4. Multi-scale simulation methodology

Figure 3 shows the multi-scale procedure followed to model the RTM process. The procedure features four steps, namely: (**S1**) identification of the polymer resin constitutive model parameters; (**S2**) identification of the effective tows behaviour at the micro-scale; (**S3**) identification of the ply's effective behaviour at the meso-scale; (**S4**) simulation of the whole RTM process with homogenized properties.

We developed a new constitutive parameters identification procedure that addresses the limitations described in Section 2.2.1. The procedure is of sufficient generality to deal with fully anisotropic constitutive theories while meeting thermodynamics restrictions. We therefore applied our procedure to identify the constitutive theory parameters for the matrix, the tows and the whole composite ply.

10

We begin with the identification the neat resin constitutive behavior by fitting the DMA, TMA and PvT-HADDOC data to the model of Equations (4) and (12). The obtained matrix behaviour during the curing cycle was programmed into ABAQUS' UMAT subroutine and input into a homogenization procedure to predict the tow's behavior. The viscoelastic response was simulated with FEM while the thermal and shrinkage properties were computed from an analytical model. The numerically predicted tows viscoelastic response was best fitted with Equation (4) and both the tows viscoelastic and expansional constitutive theories were programmed into ABAQUS' UMAT and UEXPAN subroutines. These subroutines were input into a meso-scale model where the tows and matrix were explicitly represented. This model yielded anisotropic viscoelastic responses that were best fitted again with Equations (4) and (12) and programmed into UMAT and UEXPAN subroutines. These subroutines were input into a homogeneous model to simulate the RTM process and hence predict stresses and strains during the curing and post-curing phases.

4.1. Optimization procedure to obtain the parameters of constitutive theory (4)

The developed procedure optimizes the model parameters minimizing the cost function r_a, according to:

$$
\begin{array}{c}
\arg\min_{a_1, b_1, a_2, b_2, \mathbf{C}^{(k)}, \mathbf{K}_1, \mathbf{K}_2} \quad r_a = \sum r_{ij}
\end{array}
$$

$$
\text{s.t.} \qquad
\begin{aligned}
&\mathbf{C}^{(k)} && \text{positive semi-definite,} \\
&\mathbf{K}_1, \mathbf{K}_2 && \text{positive definite,} \\
&E_{a1}, E_{a2} && > 0, \\
&\mathbf{C}^{(k)}, \mathbf{K}_1, \mathbf{K}_2 && \text{symmetric, with}
\end{aligned}
\tag{13a}
$$

$$
r_{ij} = \frac{\sum_{z=1}^{M} \left(\sigma_{ij}(t_z) - s_{ij}(t_z) \right)^2}{\sum_{z=1}^{M} \left(s_{ij}(t_z) \right)^2}, \quad (i, j = 1, 2, 3, 4, 5, 6),
\tag{13b}
$$

where M is the total number of discrete times, $\sigma_{ij}(t)$ are the stress tensor components predicted by Equation (4) at times t_z, and $s_{ij}(t)$ are the stress tensor components to be fitted by Equation (4) (either experimentally measured or numerically predicted).

Recall that all tensors in Equation (4) must be symmetric. Moreover, tensors $\mathbf{C}^{(k)}$ must be positive semi-definite, and tensors $\mathbf{K}_1$ and $\mathbf{K}_2$ must be positive definite. Let us introduce the Cholesky decomposition of these matrices as:

$$
\frac{1}{\tau_k} \mathbf{C}^{(k)} = \mathbf{L}_2^{(k)} : \left(\mathbf{L}_2^{(k)} \right)^T
\tag{14a}
$$

$$
\mathbf{K}_1 = \mathbf{L}_{K_1} : \left(\mathbf{L}_{K_1} \right)^T
\tag{14b}
$$

$$
\mathbf{K}_2 = \mathbf{L}_{K_2} : \left(\mathbf{L}_{K_2} \right)^T.
\tag{14c}
$$

Then, optimizing a_1, b_1, a_2 and b_2, as well as the components of $\mathbf{L}^{(k)}$, $\mathbf{L}_{K_1}$ and $\mathbf{L}_{K_2}$ meets the essential thermodynamics restrictions by construction and constrained only by positive activation energies $E_{a1}, E_{a2} > 0$.

It is important to note that parameters a_1, b_1, a_2 and b_2 were assumed to be fixed to those obtained for the neat polymer and therefore remained scalars when the composite was considered.

Also, the number and values of τ_k were fixed *a priori*. The procedure begins by providing initial guesses to the variables. Reasonably good initial guesses for variables a_1, b_1, a_2 and b_2 were obtained using the Time-Temperature Superposition principle (TTS). According to the TTS principle, each individual isothermal relaxation curve (taken from experiment) was automatically shifted with respect to the reference temperature along the logarithmic time scale to construct a master curve. The obtained shift factors and Arrhenius relationship (5) were used to find the initial guesses for a_1, b_1, a_2 and b_2. We were unable to devise a strategy to define relevant initial guesses for the tensor variables.

Once initial guesses were provided, the developed procedure optimized all components at once. The number of independent components for each decomposition tensor (e.g. $\mathbf{L}_{K_1}$ in Equation 14) is similar to the decomposed tensor (e.g. $\mathbf{K}_1$ in Equation 14) for the cases of general anisotropy (21 components), orthotropy (9 components) and isotropy (2 components). However, in the case of transverse isotropy, the decomposition and decomposed tensors do not have the same symmetry. The decomposition tensor differs from the orthotropic case only by the equality of diagonal components 55 and 66, thus reducing the number of independent components to 8.

The optimization procedure selected the number of independent parameters based on the optimized material symmetry determined by the user. For example, if one needs to find the parameters of the analytical viscoelastic model for an orthotropic composite material with 14 relaxation times, the developed procedure optimizes 148 parameters: 9×14 for $\mathbf{L}^{(k)}$, 2×9 for $\mathbf{L}_{K_1}$ and $\mathbf{L}_{K_2}$. The optimization procedure requires a robust algorithm that can deal with large amount of parameters, that can ensure global minima and doesn't require accurate initial guesses. The Nonlinear Optimization by Mesh Adaptive Direct Search (NOMAD 3.9.1 released in 2018-07) algorithm was used for that purpose [55].

4.2. Matrix behavior prediction (S1)

Mechanical strains

We used the multi-temperature relaxation data of Courtois et al. [16] and completed it with the measurements above T_g using the procedure given in Section 2.2.1. The entire load history was used to optimize constitutive model parameters given in Equation (4).

The DSC was performed to characterize the glass temperature with respect to the degree of cure using DiBenedetto equation (6).

Expansional strains

The CTE and CCS of the polymer matrix were experimentally measured for the set of temperatures $T = 23, 53, 150, 160, 172, 180°C$ using the TMA and the PvT-HADDOC device, respectively. The CTE and CCS were assumed to vary linearly with respect to the temperature.

4.3. Tows behavior (S2)

Mechanical strains

The tows packing was assumed to be hexagonal in warp and weft directions and containing 70% and 75% of carbon fibers, respectively. Figure (4) shows examples of RVEs of warp and weft tows generated in ABAQUS. The carbon fibers were assumed to be linearly elastic and transverly isotropic ($E_1 = E_2 = 10\,300$ MPa, $E_3 = 276\,000$ MPa; $\nu_{12} = 0.3$, $\nu_{23} = \nu_{31} = 0.0097$; $G_{12} = 3\,960$ MPa, $G_{23} = G_{31} = 27\,900$ MPa) and the resin obeyed the temperature and cure-dependent linearly viscoelastic behavior model of Equation (4) obtained from S1. Next, a set of six isothermal strain load cases was applied (three uniaxial tension and three shear for each degree of cure) to compute the homogenized response against which Equation (4) was best fitted using the developed optimization
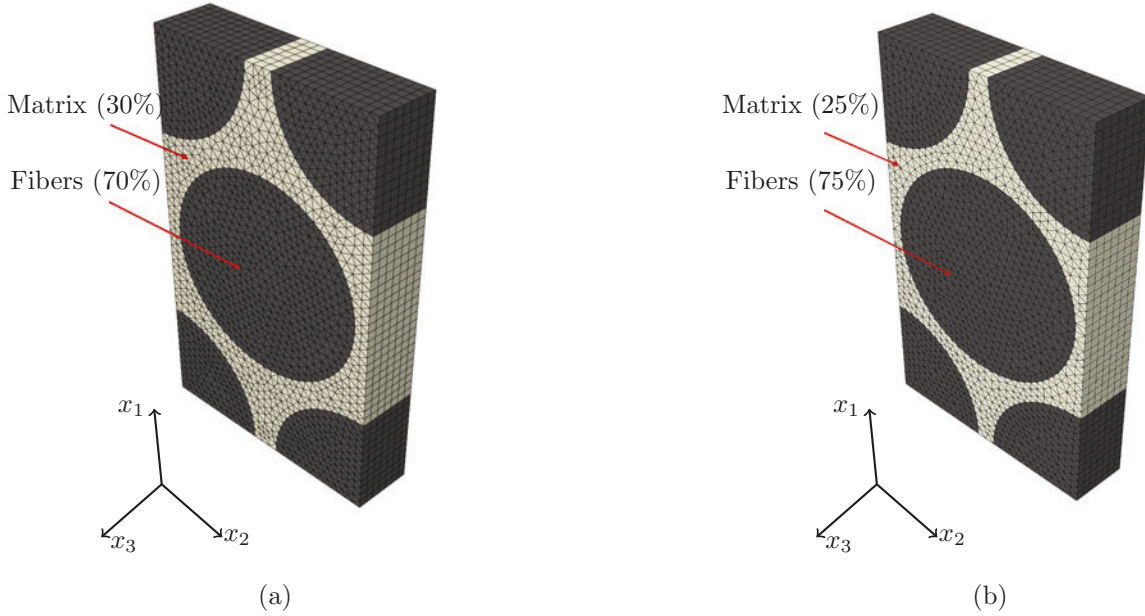
Figure 4: Example of micro-scale RVEs meshed with 19 698 6-node linear triangular prism elements exhibiting carbon fibers volume fractions of: (a) 70% corresponding to the warp tow; (b) 75% corresponding to the weft tow

procedure (Section 4.1) to obtain the tows effective viscoelastic behavior. The homogenization procedure is detailed in Appendix A.

We simulated 90-minute FE relaxation tests for each unit load case for $\alpha = 1, 0.9, 0.8$ and for the different temperatures ranging from 30°C to 180°C with a step size of 15°C.

Expansional strains

The composite effective CTE and CCS were computed using the Mori-Tanaka micro-mechanical scheme according to the formulas given in Appendix B.

4.4. Ply behaviour (S3)

Mechanical strains

Figure 5(a) shows the 3D interlock woven RVE architecture constructed with WiseTex [56]. Weft tows, warp tows and the matrix accounted for 43.6%, 32.8%, 23.6% of the whole volume, respectively. The neat polymer and tows were assumed to obey the temperature and cure-dependent linearly viscoelastic behavior described by Equation (4) with the previously optimized model parameters against experimental data (DMA for the polymer) and numerical homogenization data (FEM homogenization for the tows), respectively.

The homogenization was carried out with Mixed Uniform Boundary Conditions (MUBC) [57]. We simulated 90-minutes FE relaxation tests for each unit load case (see Appendix C for the boundary conditions) for $\alpha = 1$ and 0.9 at an assumed temperature of 90°C. The parameters of constitutive Equation 4 were determined from the optimization procedure described in Section 4.1 to best fit the simulated relaxation curves. As was done for the tows, we assumed that the temperature dependency was the same as that of the resin and, thus, only the simulations for a single temperature were required.
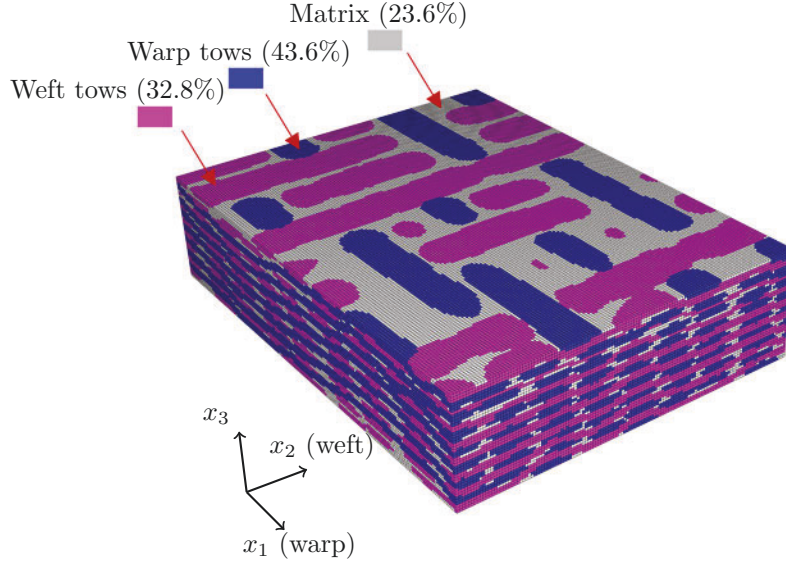
13

Figure 5: Example of the numerical RVE for the whole composite featuring 982 800 linear 8-node brick elements

Expansional strains

The effective CTE was obtained by applying a uniform unit increase in temperature at $T = 23, 53, 150, 160, 172, 180°C$ for $\alpha = 1, 0.9$. The surfaces of the RVE were assumed to be stress free. The strain tensor was averaged using the same principle as in Equation A.1. The numerically obtained effective CTE behavior was interpolated with a piecewise linear function as:

$$\boldsymbol{\theta}(T) = \begin{cases} \boldsymbol{\theta}_1^1 T + \boldsymbol{\theta}_2^1, & T_1 < T \leq T_2 \\ \boldsymbol{\theta}_1^2 T + \boldsymbol{\theta}_2^2, & T_2 < T \leq T_3 \\ \boldsymbol{\theta}_1^3 T + \boldsymbol{\theta}_2^3, & T_3 < T \leq T_4 \\ \boldsymbol{\theta}_1^4 T + \boldsymbol{\theta}_2^4, & T_4 < T \leq T_5 \\ \boldsymbol{\theta}_1^5 T + \boldsymbol{\theta}_2^5, & T_5 < T \leq T_6 \end{cases} \tag{15}$$

where $\boldsymbol{\theta}_t^s$ are adjustable parameters where $s = 1, 2, 3, 4, 5$ and $t = 1, 2$, T_f are the temperature points at which simulations were performed where $f = 1, 2, 3, 4, 5, 6$.

The effective CCS was obtained similarly by imposing local CTEs that yielded the same shrinkage as that associated with curing when a unit and uniform temperature profile is applied. The numerically obtained effective CCS tensor behavior was fitted with a piecewise linear function as:

$$\boldsymbol{\beta}(T) = \begin{cases} \boldsymbol{\beta}_1^1 T + \boldsymbol{\beta}_2^1, & T_1 < T \leq T_2 \\ \boldsymbol{\beta}_1^2 T + \boldsymbol{\beta}_2^2, & T_2 < T \leq T_3 \\ \boldsymbol{\beta}_1^3 T + \boldsymbol{\beta}_2^3, & T_3 < T \leq T_4 \\ \boldsymbol{\beta}_1^4 T + \boldsymbol{\beta}_2^4, & T_4 < T \leq T_5 \\ \boldsymbol{\beta}_1^5 T + \boldsymbol{\beta}_2^5, & T_5 < T \leq T_6 \end{cases} \tag{16}$$

where $\boldsymbol{\beta}_t^s$ are adjustable parameters where $s = 1, 2, 3, 4, 5$ and $t = 1, 2$.

The effective mechanical response of the composite was programmed into ABAQUS' UMAT subroutine while the expansional strains were programmed into the UEXPAN subroutine. Together, subroutines describe the optimized time-temperature- and cure-dependent mechanical model required to simulate the whole RTM process.
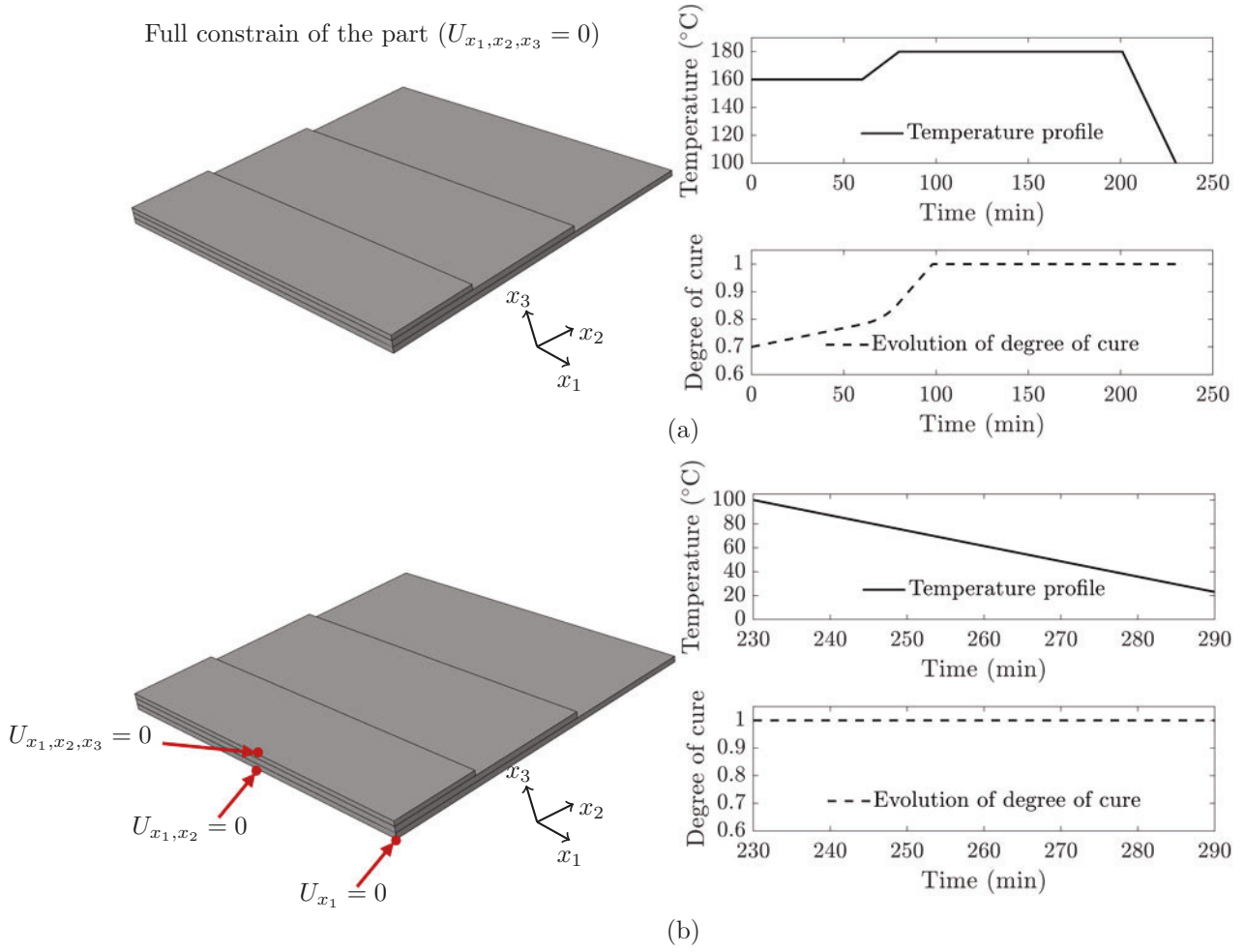
Figure 6: Schematic boundaries conditions, temperature profile and degree of cure as a function of time for: (a) the in-mold and (b) the out-of-mold stages for the RTM manufacturing simulation of a non-flat plate reinforced with a 3D interlock woven fabric

4.5. RTM process simulation (S4)

The RTM process was simulated by creating the FE representation of the part geometry and by accounting explicitly for the plies orientations and thickness. The simulation procedure of the manufacturing process described in Section 3 involved two phases that required different sets of boundary conditions, namely: (1) in-mold and (2) out-of-mold.

During the in-mold phase, the part was submitted to:

- Fully clamped nodal displacements $(U_{x_1}, U_{x_2}, U_{x_3} = 0)$ on the exterior surfaces;

- A uniform temperature at every node. The temperature followed the time variation shown in Figure 6(a);

- A uniform degree of cure at every integration point in the form of a solution independent variable. The time-variation of the degree of cure is shown in Figure 6(a). The degree of cure was obtained by using Equation (2) with the temperature profile of Figure 6(a).

During the out-of-mold phase, the composite part was submitted to the following constraints:
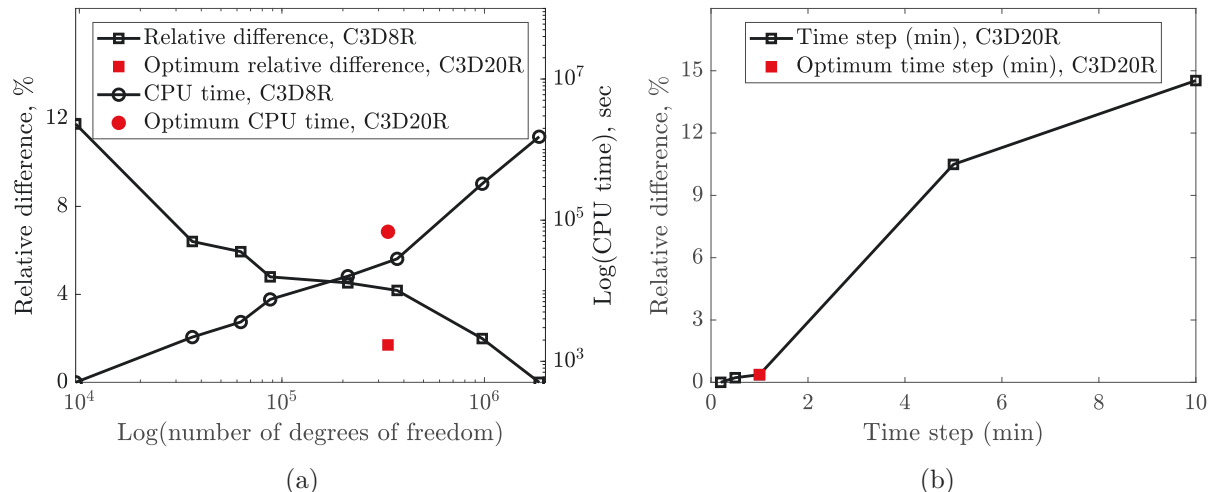
15

Figure 7: Convergence study for simulating the RTM process: (a) the relative difference (%) of the maximum displacement predictions with respect to those of the finest mesh are plotted against CPU time and the number of degrees of freedom; (b) the relative difference (%) of the maximum displacement predictions with respect to those with the smallest time step

- Free standing conditions as shown in Figure 6(b) that prevented rigid body motions;

- A uniform temperature at every node. The temperature followed the time variation shown in Figure 6(b).

FEM model and convergence analysis

A convergence analysis, based on the computed maximum magnitude of displacement, was performed to identify the optimal number and type of elements, as well as the time increment for simulating the RTM manufacturing process.

We performed nine simulations of the RTM process where the number and type of elements varied while the time step was fixed ($\Delta t = 1$ (min)). The relative difference of the maximum displacement predictions with respect to those of the finest mesh ($\sim 539\,000$ linear 8-node brick elements C3D8R) against CPU time and the number of degrees of freedom are presented in Figure 7(a). We deemed that 24 000 quadratic 20-node brick elements (C3D20R) yielded sufficiently accurate results for a reasonable computational time. For the selected number and type of elements, a set of simulations with different time steps ($\Delta t = 0.2, 0.5, 1, 5, 10$ (min)) were performed. Figure 7(b) shows the relative difference of the maximum displacement predictions with respect to those with the smallest time step. The results suggest that a time step of $\Delta t = 1$ (min) yielded sufficiently accurate results.

5. Simulation results

5.1. Matrix behavior

Mechanical strains

Figure 8 shows the polymer response to the strain and temperature histories given in Section 4.2 computed from the constitutive theory (Equation (4)) with the parameters that best fitted the experimental data reported in [16] and completed by the new data above T_g generated in our work. In total, 14 relaxation times distributed uniformly on a logarithmic scale were used.
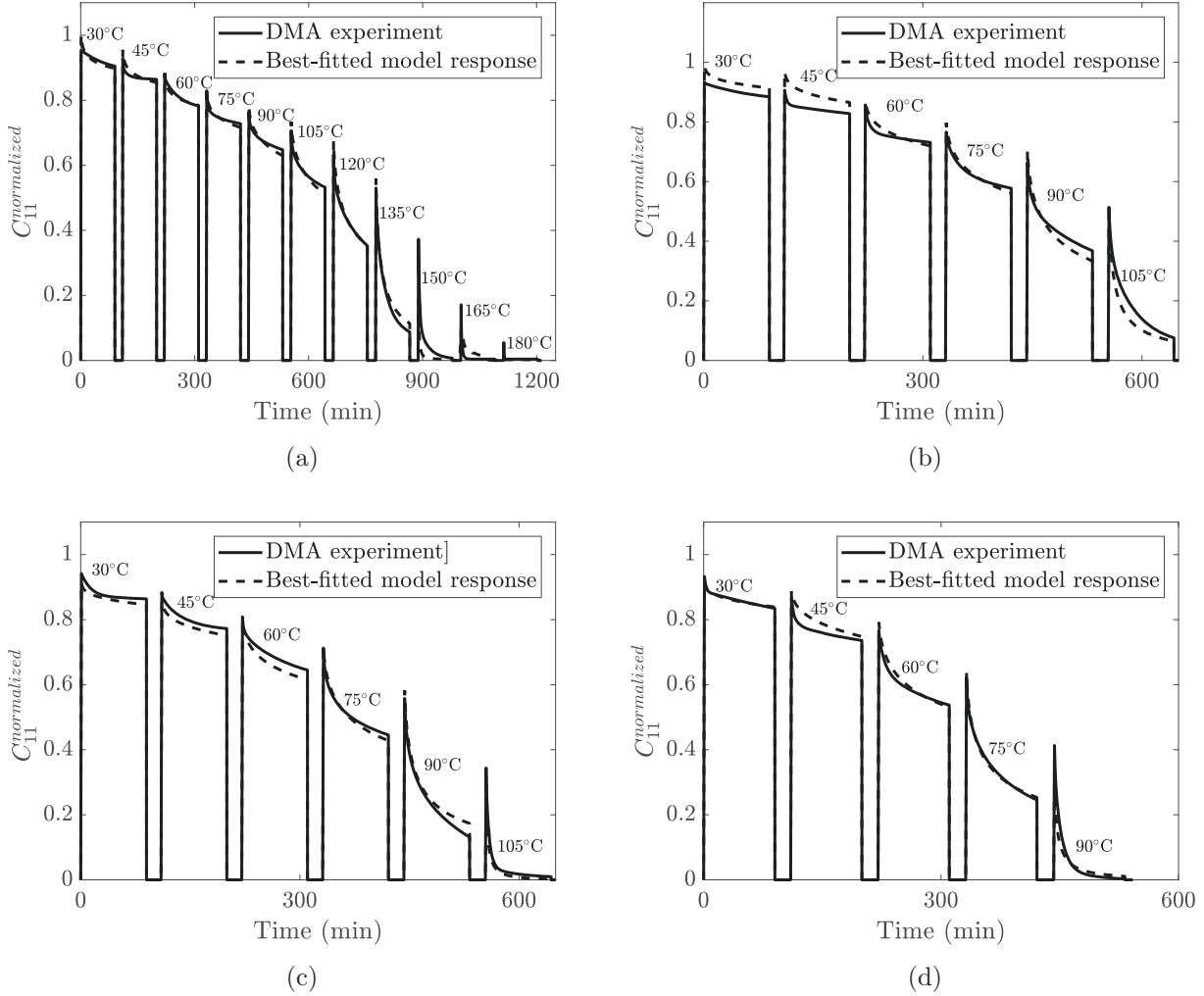
Figure 8: Temperature- and degree of cure-dependent best fitted model predictions against DMA experimental curves for the pure polymer matrix exhibiting a degree of cure of: (a) 100 %; (b) 90%; (c) 85%; (d) 80%

Expansional strains

The experimentally obtained CTE and CCS are presented in Figure 9 along with the piecewise linear functions that were used to interpolate these coefficients.

5.2. Tows behavior

Mechanical strains

We assumed a transversely isotropic behavior for the tows to reduce the number of parameters subjected to the optimization and save the computational time. The discrepancy between the FE predictions of the effective stiffness components from an assumed symmetry was computed as the relative error between the corresponding components of the instantaneous stiffness tensor $\left(\frac{C_{44}^{inst} - 0.5(C_{11}^{inst} - C_{12}^{inst})}{C_{44}^{inst}} \right) \times 100\%$. The maximum error was found to be 1.5% for $\alpha = 0.8$ at 180°C, which is deemed acceptable to assume a transversely isotropic behavior of the tows.

Figure 10 shows the homogenized responses computed from the RVEs as well as the computations from constitutive Equation 4 whose parameters best-fitted the homogenized response. Overall, 14 relaxation times evenly distributed on a logarithmic scale were used, which led to 128 parameters to
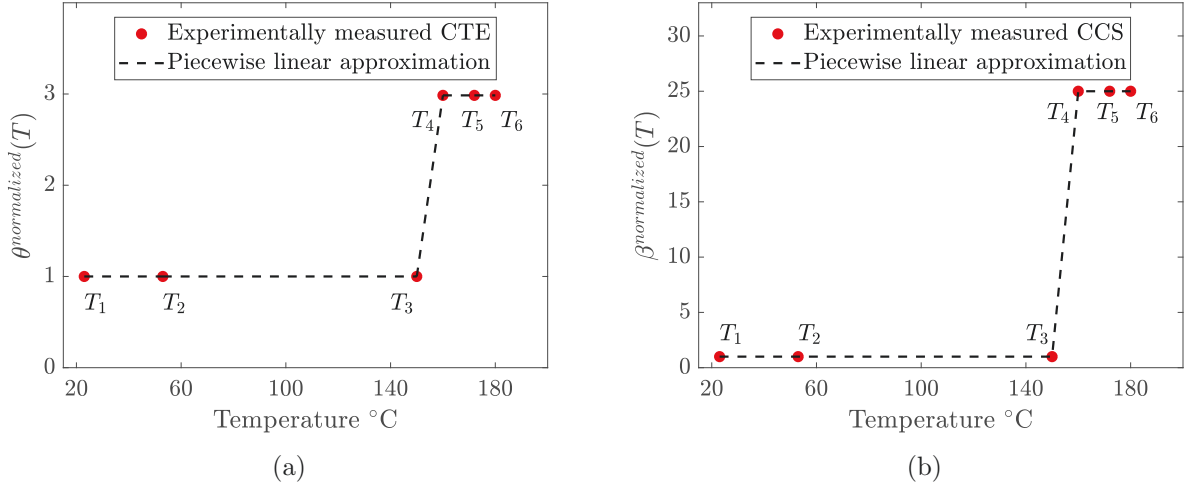
17

Figure 9: Experimentally measured properties of the neat polymer fitted with a linear piecewise function: (a) CTE; (b) CCS

be identified. Recall that a_1, b_1, a_2 and b_2 were not optimized and their values were those obtained for the neat resin. This choice was made to reduce the optimization cost and since it yielded an accuracy deemed acceptable.

The accuracy of the best fitted model predictions was found to be satisfactory with the maximum relative error being less than 5% for all times. This discrepancy could partially be explained by the transversely isotropic behaviour assumption and the number of relaxation times that could be increased for better accuracy. Optimizing the relaxation times could also further improve the best fitting adequacy.

5.3. Ply behavior
Mechanical strains

The 3D composite was assumed to exhibit an anisotropic behavior with 10 independent non-zero components of stiffness tensor. A component was deemed negligible when its ratio to the component having the largest value was below 0.01.

Figure 11 presents the comparison between the normalized components of the stiffness tensors computed numerically and those obtained from the constitutive model with the optimized parameters (Equation 4). Overall, 14 relaxation times evenly distributed on a logarithmic scales were used, which led to 160 parameters to be identified. Similarly to the simulation at the micro-scale, a_1, b_1, a_2 and b_2 were not optimized and their values were set to those of the neat polymer.

For every component, and for all times, the relative difference between the RVE prediction and the best fitted constitutive model was lower than 1%.

Expansional strains

Figure 12 depicts the homogenized components of the composite's CTE and CCS computed at the specified temperatures (Section 4.4) along with the linear piecewise functions that were used to estimate coefficients (Equations (15) and (16)).

5.4. RTM process simulation

Figure 13(a) depicts the optimized FE mesh of the non-flat composite part and shows the local orientations of plies 1 to 3. For example, $x_1^{''}$ and $x_2^{''}$ are the local warp and weft directions of
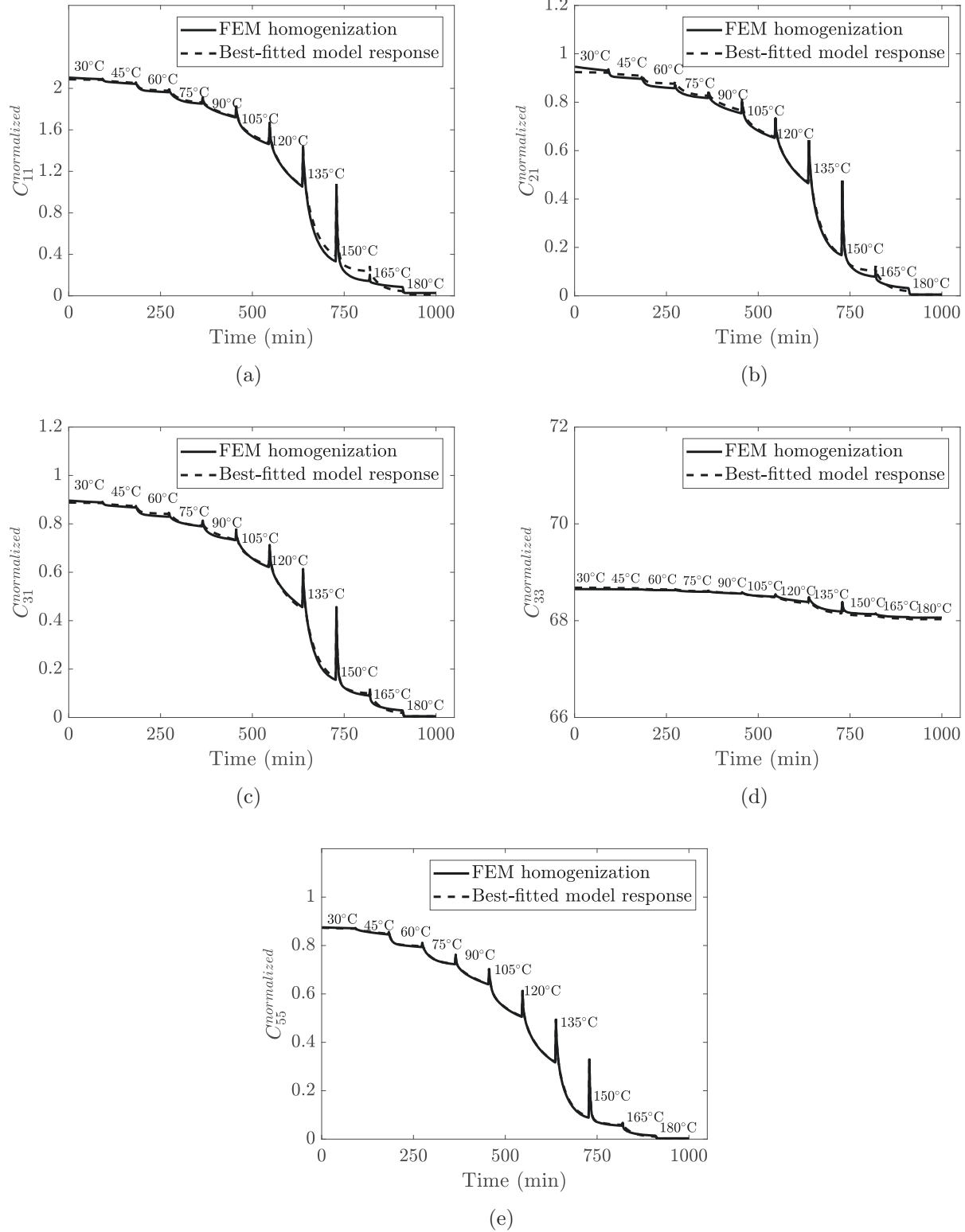
Figure 10: Components of the normalized stiffness tensors obtained using the best-fitted temperature- and degree of cure-dependent model against FEM homogenization at the micro-scale for $\alpha = 1$ and volume fraction of fibers equal to 70%: (a) C_{11}, (b)C_{21}, (c) C_{31}, (d) C_{33} and (e) C_{55}
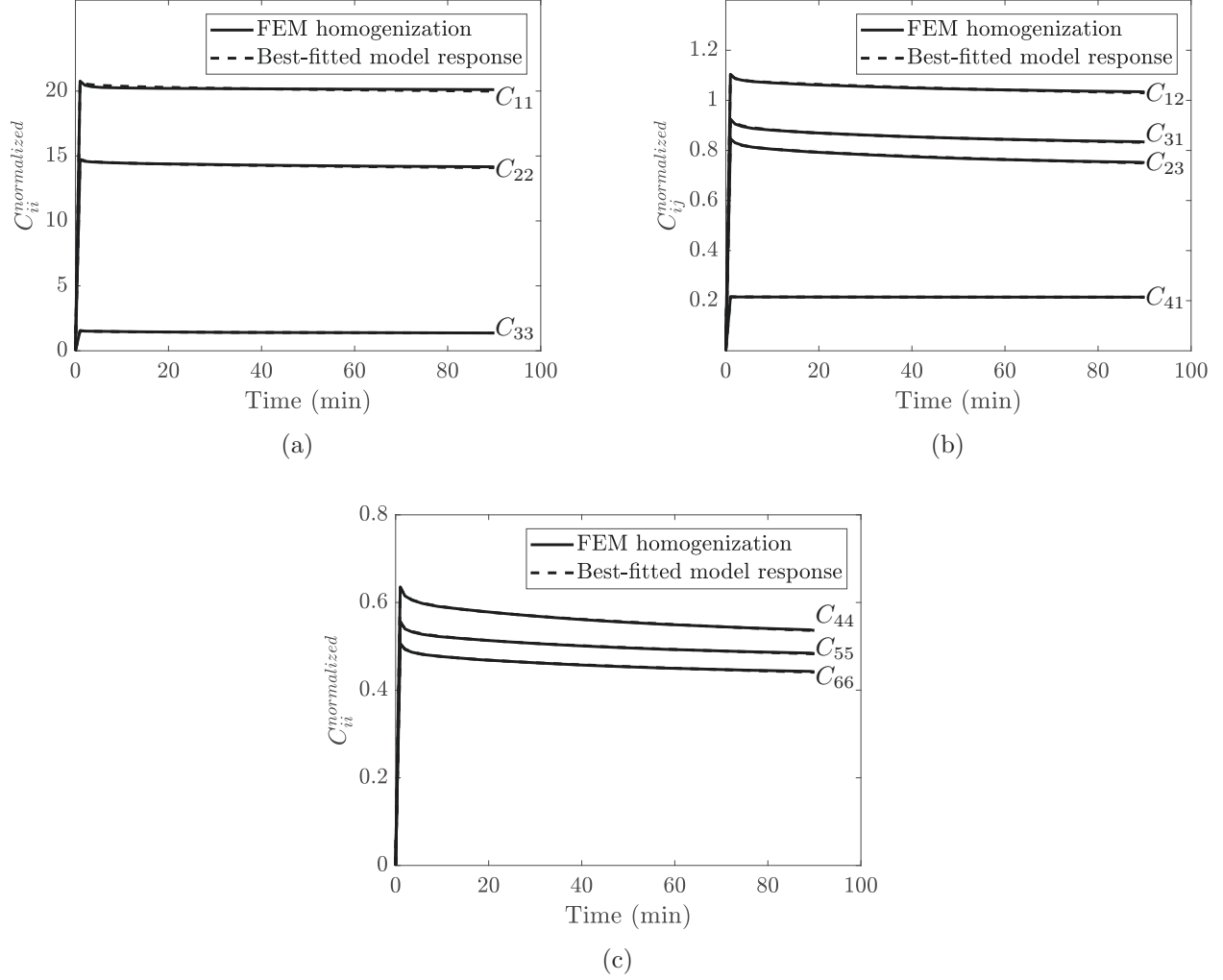
19

Figure 11: Relaxation curves obtained using the homogenized temperature- and degree of cure-dependent model against FEM homogenization at the meso-scale for $\alpha = 1$: (a) C_{ii}, $i = 1, 2, 3$; (b) C_{ij}, $i = 1, 2$, $j = 2, 3$, $i \neq j$; (c) C_{ii}, $i = 4, 5, 6$

ply 2 that are rotated by 45° with respect to the global reference frame. Figures 13(b-d) present the predicted displacement fields using the FEM model with the parameters identified from the convergence study. Figure 13(d) shows that the through the thickness warpage u_3 (along the x_3 direction) is larger, when compared to the in-plane distortions u_2 and u_1 (along x_2 - weft and x_1 - warp, respectively). The predicted distortion along x_2 is higher than that along x_1. These observations can be explained by the fact that the effective stiffness tensor component C_{33} is lower than C_{22}, which is itself lower than the C_{11} component (see Figure 11). The highest levels of distortion were obtained at the corners with the maximum absolute value being located at the lower right corner of the thinnest section of the part. This observation results from the orientation of ply 2 (45 °) having its local weft axis x_2'' aligned towards that corner and the fact that stiffness tensor component C_{22} along this direction is lower than that along the warp direction C_{11} due to the weaving pattern of 3D the fabric.
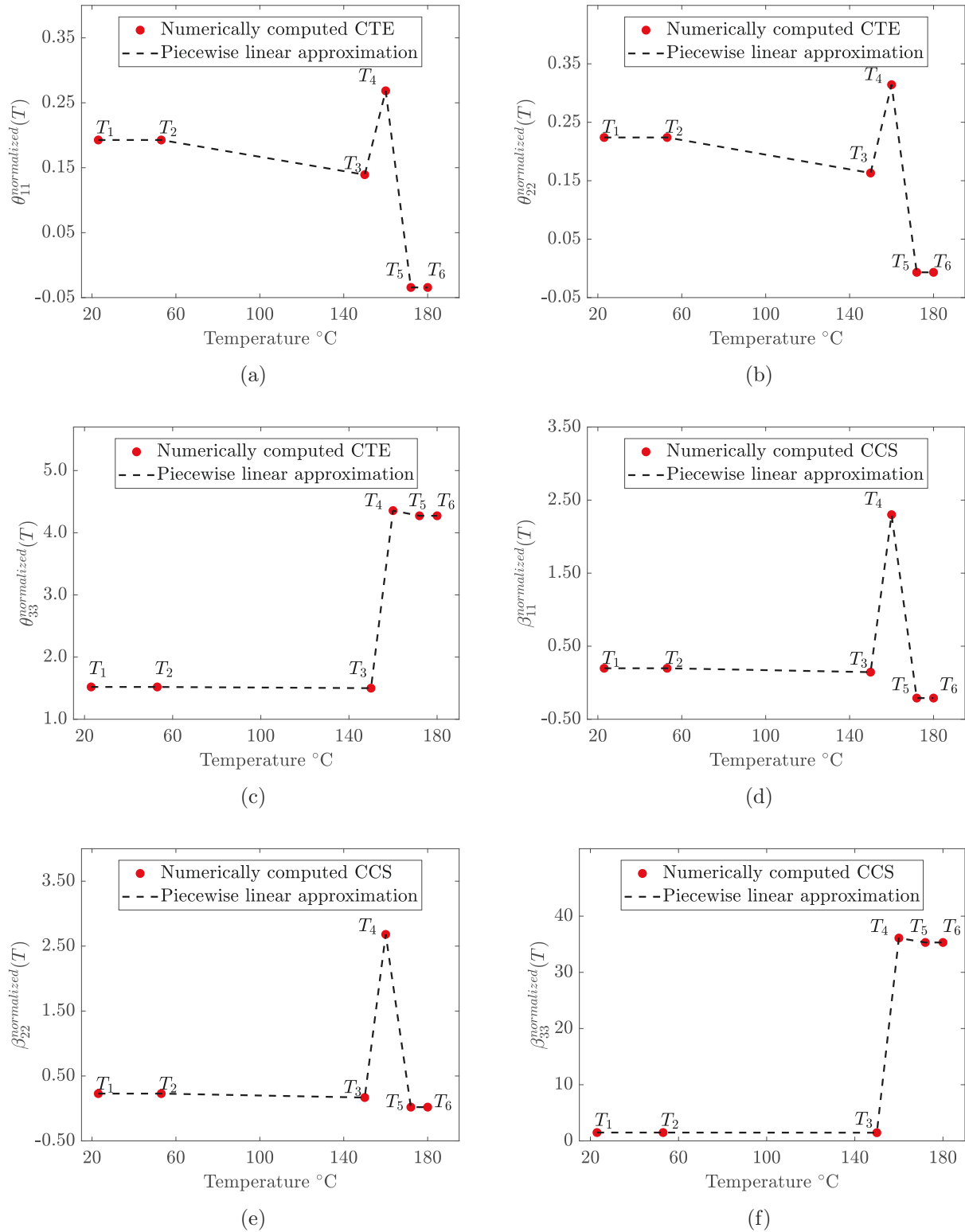
20

Figure 12: Components of the ply's effective CTE and CCS computed using numerical homogenization and approximated with piecewise linear functions: (a)θ_{11} ;(b)θ_{22}; (c)θ_{33}; (d)β_{11} ;(e)β_{22}; (f)β_{33}

6. Comparison between the distortion predicted with the proposed multi-scale simulation and that experimentally measured

The nominal (ideal) CAD model of the part was generated with respect to the known specifications (size of the mold and spacers) and was used as a reference (zero distortion). The CAD model
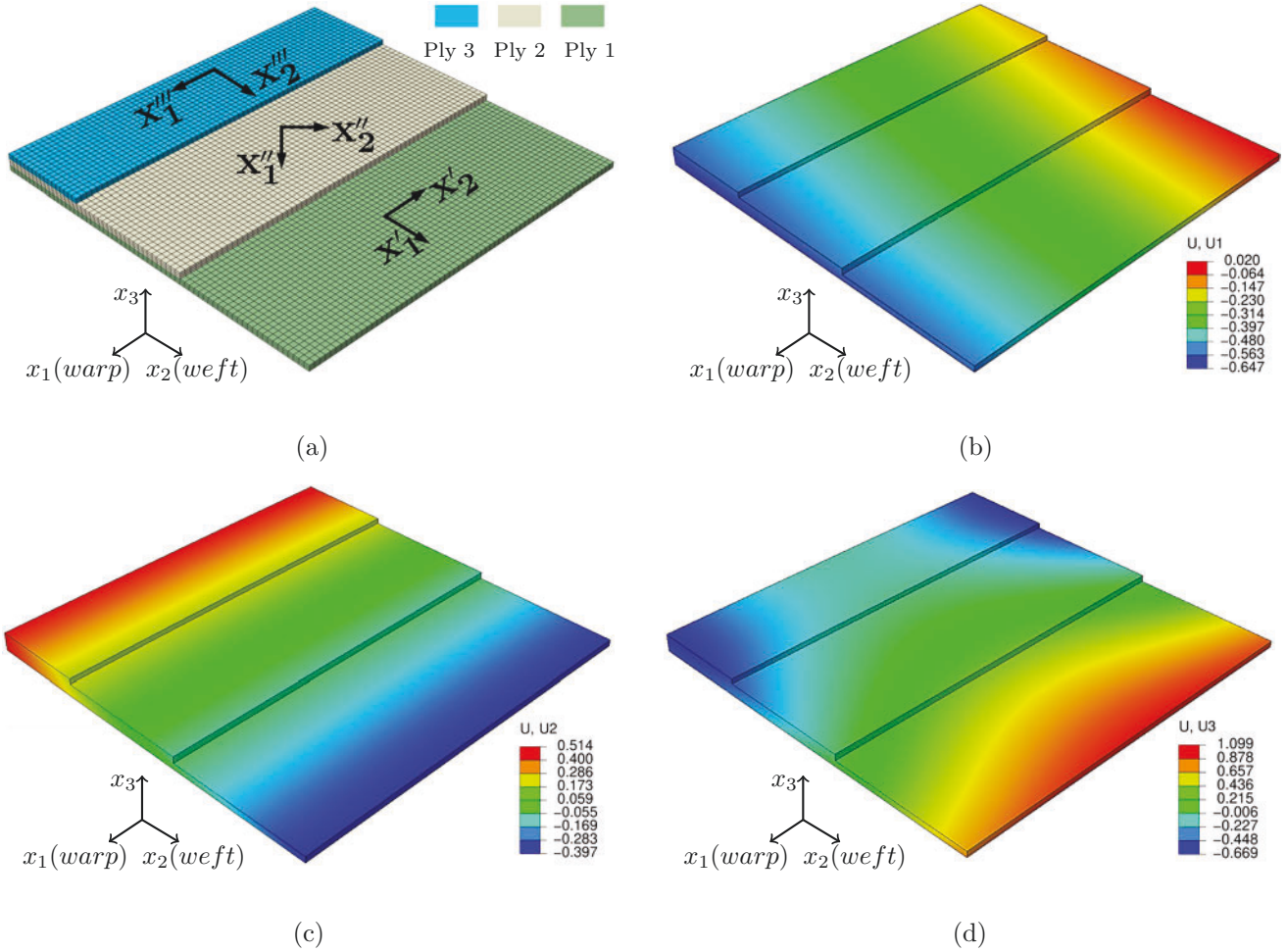
Figure 13: Numerical prediction of distortion (mm) for the RTM manufactured specimen: (a) FE mesh consisting of $\sim 24\,000$ quadratic 20-node brick elements C3D20R; (b) displacement in x_1 direction; (c) displacement in x_2 direction; (d) displacement in x_3 direction

was imported to the GOM Inspection Software which generated the surface mesh containing the so-called nominal elements. Next, the reconstructed surface containing the so-called actual elements (Section 3) was also imported to the GOM Inspection Software. Since the reconstructed 3D object had a different spatial orientation, we aligned the reference and the reconstructed surfaces. The software linked nominal and actual elements to compute distortions. We then substituted the reconstructed surface with that predicted by our simulation procedure and repeated the procedure to compute distortions obtained from the RTM process modelling.

Figure 14(a) shows the numerically predicted distortion contour plot while Figure 14(b) presents the experimentally observed distortion of the manufactured part. The maximum absolute distortion was observed in the lower right corner of the thinnest part of the part and it was positive for both the numerical analysis and the experimental data. The negative values of distortions were obtained mainly at the thickest section of the step-wise plate with the lower values being located at the right corner. In the middle of the part, the absolute displacement values are close to zero since it tends to compensate for the negative and positive distortion values. The displacements are also plotted along specific paths in Figure 14 to allow for a better comparison.

Figures 15(a)-(f) compare the numerically predicted distortion against that experimentally
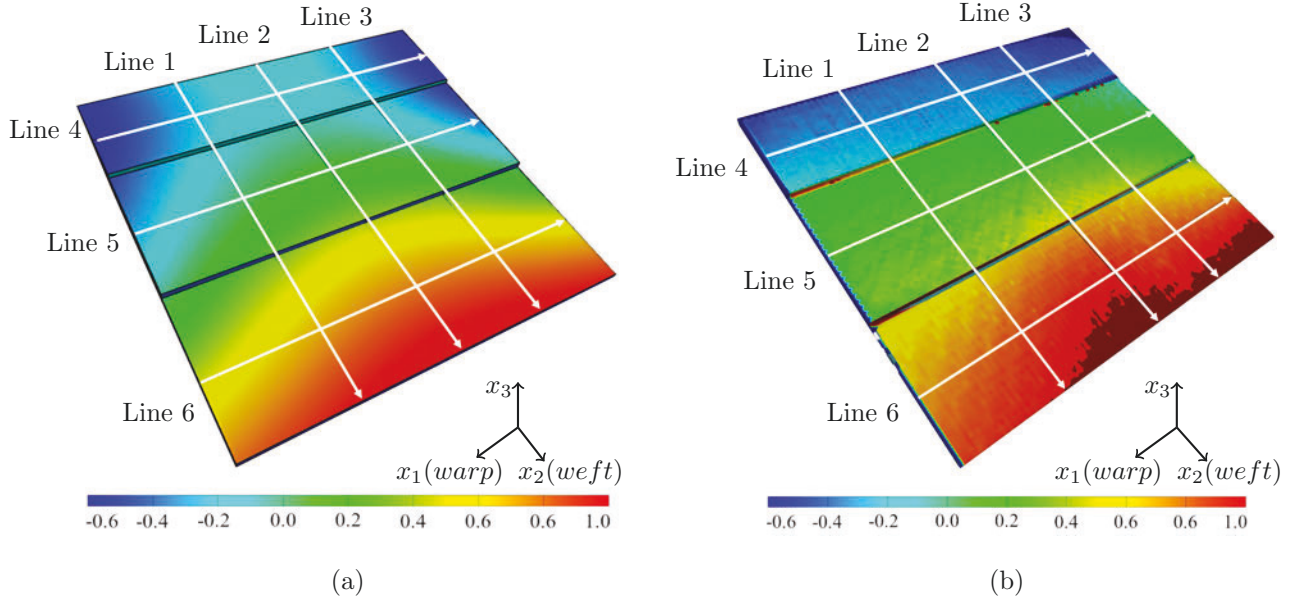
22

Figure 14: Distortion (mm) contour plots obtained from: (a) our simulation procedure and (b) the actual RTM manufacturing and subsequent measurements. The lines 1-6 indicate the paths along which distortion are plotted for comparison

measured. Along the longitudinal lines (1-3), the FE simulation was able to approximate the experimental response qualitatively, reproducing the evolution of the distortion from one ply to another. The proposed numerical approach quantitatively estimated maximum absolute distortion along all these three lines with the relative error being lower than 2.8%. The maximum discrepancy was in ply 2 where the lowest absolute values of distortion were observed for both the simulations and the measurements. Along the transverse lines (4-6), the model qualitatively estimated the distribution of the distortion within the plies. The worst discrepancy between the predictions and measurements was, again, in ply 2. In the thinnest ply 1 and along the line 6, the multi-scale simulation quantitatively predicted warpage with a mean relative error of 13%.

7. Discussion

The developed multi-scale FE simulation of the whole RTM process was able to qualitatively estimate manufacturing induced distortion in a non-flat 3D woven composite capturing its evolution with respect to the variations in properties and thickness. The simulation quantitatively predicted the maximum absolute distortion in the whole part and the distribution of warpage in the thinnest part of the specimen. However, in some cases, we were unable to quantitatively predict the distortion. Indeed, the quantitative comparison was not reliable in poorly reconstructed contours of the lateral surfaces when changing from one ply to another (examples of reconstruction artefacts are given in Figure 2 (b)). The largest discrepancy between numerical estimations and measurements was observed in ply 2. This observation could be explained by the fact that the distortion in this area is close to the equipment sensitivity.

Overall, obtaining distortion from the reconstructed surface is sensitive to its alignment with an "ideal" CAD model (zero warpage). Inducing larger distortion would have limited this effect. The discrepancies could come from the difference between our idealized RVE and the actual manufactured part that could exhibit local tows disorientation. Moreover, the fiber volume fraction of warp and weft tows could be slightly different from the idealized RVE. Also, the effective CTE
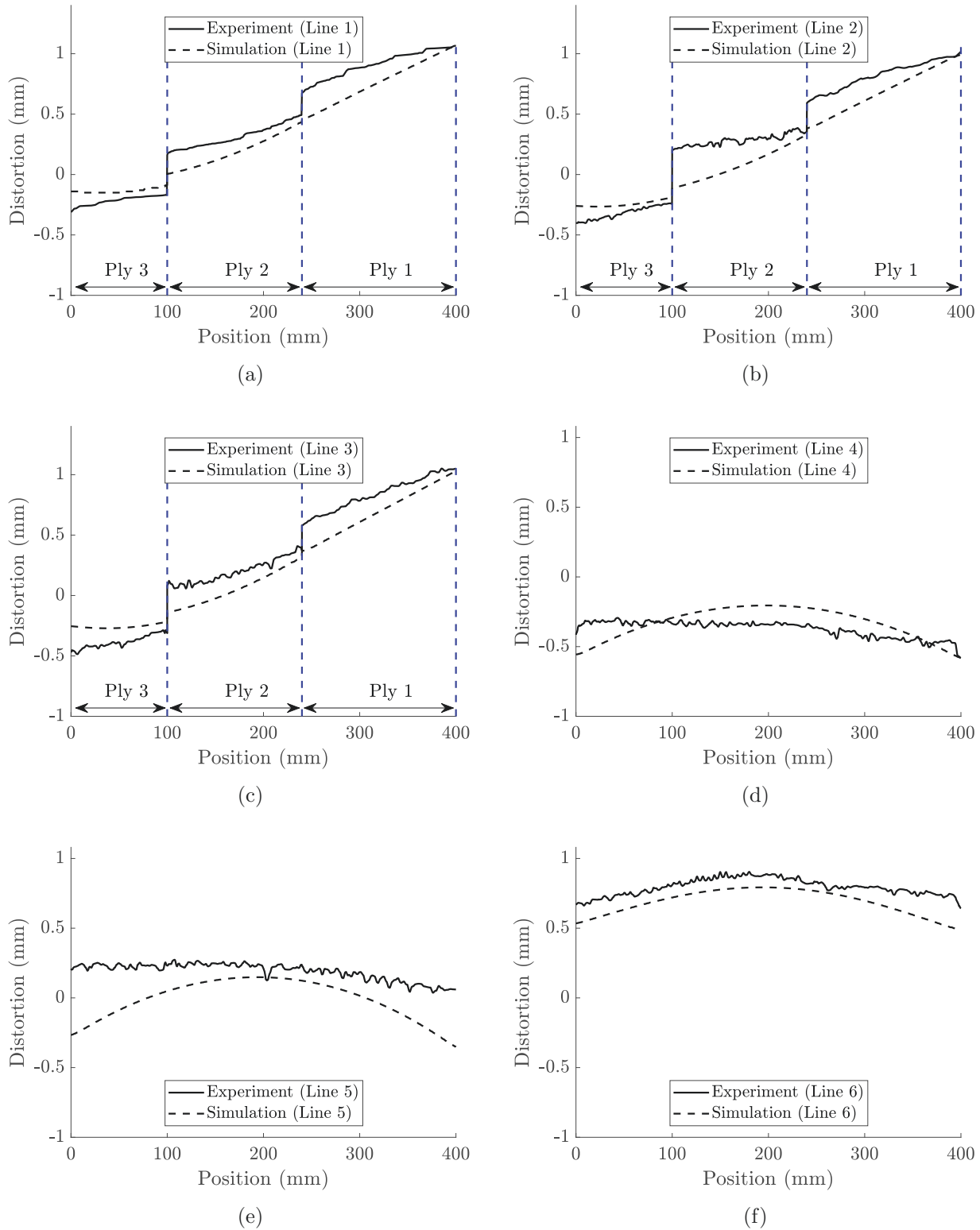
Figure 15: Comparison of the distortion distribution computed numerically against that experimentally measured along the lines shown in Figure 14: (a) Line 1; (b) Line 2; (c) Line 3; (d) Line 4; (e) Line 5; (f) Line 6

and CCS were approximated with piecewise functions that neglect a non-linear behaviour. The discrepancy could also come from the relaxation tests on the neat resin. Indeed, performing tests

24

close to and, especially, above the glass transition temperature presents a serious challenge.

8. Conclusion

This study demonstrated the multi-scale identification procedure of a 3D woven composite anisotropic thermo-chemo-mechanical constitutive model parameters below and above T_g. The developed procedure overcomes the limitations of a previous study and presents a framework to best fit behavior of materials having various symmetries with no special adjustments. The outcome of the identification process yielded a satisfactory correspondence between best-fitted model response and experimental or numerical data, at every scale.

The obtained behavior of the 3D woven composite was used to predict the distortion of a non-flat RTM part by direct simulation of the process accounting for applied thermal cycle and evolution of degree of cure during manufacturing. The contoured geometries of the manufactured part were digitized with an optical scanner for subsequent distortion measurement. It was found that the presented approach was capable of qualitative and, in some cases, quantitative prediction with the highest accuracy $\sim 2.8\%$ of manufacturing induced geometrical distortions.

The part distortion simulations presented in this work revealed that the presented approach was capable to qualitatively and, in some cases, quantitatively, predict manufacturing induced geometrical distortions. It was also observed that the numerical approach was able to capture specific geometrical features as well as variations in thickness and properties of the part.

Further research should focus on a sensitivity analysis to measure the impacts of variation in simulation parameters on the computed distortion. The multi-scale FE simulations were conducted on idealized RVEs that may differ from the reality and, therefore, it would be of interest to investigate the influence of RVEs parameters (volume fractions of fibers etc.) on the final predictions. Also, it could be interesting to quantitatively interconnect the manufacturing parameters such as temperature cycle etc. with the final distortion for the optimization of the RTM procedure.

9. Acknowledgment

Appendix A. Details of the homogenization procedure at the micro-scale

Table A1: Prescribed strains corresponding to the six load-cases used for computing the tows effective properties

Prescribed average strain,%	Load-case					
	Tensile 1	Tensile 2	Tensile 3	Shear 12	Shear 23	Shear 31
ε_{11}^0	1	0	0	0	0	0
ε_{22}^0	0	1	0	0	0	0
ε_{33}^0	0	0	1	0	0	0
ε_{12}^0	0	0	0	1	0	0
ε_{23}^0	0	0	0	0	1	0
ε_{31}^0	0	0	0	0	0	1

The unit loadings given in Table A1 were applied on a RVE and the resulting mechanical response was computed. The homogenized stress components were obtained through spatial averaging as per:

$$\langle \sigma_{ij} \rangle_g = \frac{1}{V} \sum_{l=1}^{P} \left(\sigma_{ij}^{(l)} \right)_g, (i,j=1,2,3; m=1,2,3,4,5,6), \tag{A.1}$$

where $\langle \sigma_{ij} \rangle_g$ is the volume average of the stress component ij resulting from the application of the g-th loadcase, V is the total volume of the RVE, $\left(\sigma_{ij}^{(l)} \right)_g$ is the ij stress component at the centroid of the finite element l computed from the g-th loadcase, $V^{(l)}$ is the volume of the element l and P is the total number of elements in the model. Given the average stress components histories and applied strain, the effective stiffness tensor can be computed using a linearly viscoelastic constitutive relation. For example, after the application of the first loadcase $\varepsilon = \{\varepsilon_{11}=1; \varepsilon_{22}=0; \varepsilon_{33}=0; \varepsilon_{12}=0; \varepsilon_{23}=0; \varepsilon_{13}=0\}$ and computing σ_{11} yields C_{11}, C_{21}, C_{31}, C_{41}, C_{51} and C_{61}. This operation is carried out six times to obtain all components of a stiffness tensor.

Appendix B. Mori-Tanaka micromechanical scheme

Following [58, 59, 60], the effective CTE of a composite with parallel and identical inhomogeneities according to the Mori-Tanaka scheme can be written as:

$$\boldsymbol{\theta}^{eff} = \boldsymbol{\theta}^0 + \left[\frac{1-\phi}{\phi}\left(\mathbf{S}^0 : \mathbf{N} : \mathbf{S}^0\right)^{-1} + \left(\mathbf{S}^1 - \mathbf{S}^0\right)^{-1}\right]^{-1} : \left(\mathbf{S}^1 - \mathbf{S}^0\right)^{-1} : (\boldsymbol{\theta}^1 - \boldsymbol{\theta}^0) \tag{B.1}$$

where ϕ is the inhomogeneities volume fraction, $\boldsymbol{\theta}^0$ and $\boldsymbol{\theta}^1$ are the matrix and inhomogeneity CTEs, $\mathbf{N}$ is the fourth order stiffness contribution tensor of a single inclusion, $\mathbf{S}^0$ and $\mathbf{S}^1$ are the matrix and inhomogeneity compliance tensors, respectively.

In our case, the inhomogeneity is an infinitely long fiber with an axis of transverse isotropy along x_3 for which all non-zero and independent components of $\mathbf{N}$ are given as [61]:

$$N_{11} = \frac{c_1(\lambda_0 + 2G_0)}{c_1 + \lambda_0 + 2G_0} + \frac{2c_2 G_0(\lambda_0 + 2G_0)}{4G_0(\lambda_0 + 2G_0) + c_2(\lambda_0 + 3G_0)} \tag{B.2a}$$

$$N_{12} = \frac{c_1(\lambda_0 + 2G_0)}{c_1 + \lambda_0 + 2G_0} - \frac{2c_2 G_0(\lambda_0 + 2G_0)}{4G_0(\lambda_0 + 2G_0) + c_2(\lambda_0 + 3G_0)} \tag{B.2b}$$

$$N_{33} = \frac{2c_6(\lambda_0 + 2G_0) + 2(c_1 c_6 - c_3 c_4)}{2(\lambda_0 + 2G_0 + c_1)} \tag{B.2c}$$

$$N_{44} = \frac{2c_2 G_0(\lambda_0 + 2G_0)}{4G_0(\lambda_0 + 2G_0) + c_2(\lambda_0 + 3G_0)} \tag{B.2d}$$

$$N_{55} = \frac{2c_5 G_0}{8G_0 + c_5}, \tag{B.2e}$$

where λ_0 and G_0 are respectively the Lamé's first parameter and shear modulus of the matrix material, and c_e, $e = 1, 2, 3, 4, 5, 6$ are defined as:

$$c_1 = \frac{C_{11}^1 + C_{12}^1}{2} - (\lambda_0 + G_0) \tag{B.3a}$$

$$c_2 = 2(C_{44}^1 - G_0) \tag{B.3b}$$

$$c_3 = c_4 = C_{13}^1 - \lambda_0 \tag{B.3c}$$

$$c_5 = 4(C_{55}^1 - G_0) \tag{B.3d}$$

$$c_6 = C_{33}^1 - (\lambda_0 + 2G_0), \tag{B.3e}$$

where C_{mn}^1 are components of the inhomogeneity stiffness tensor.

To compute the effective CCS one should substitute in (B.1) CTEs with CCSs.

Appendix C. Details of the homogenization procedure at the meso-scale
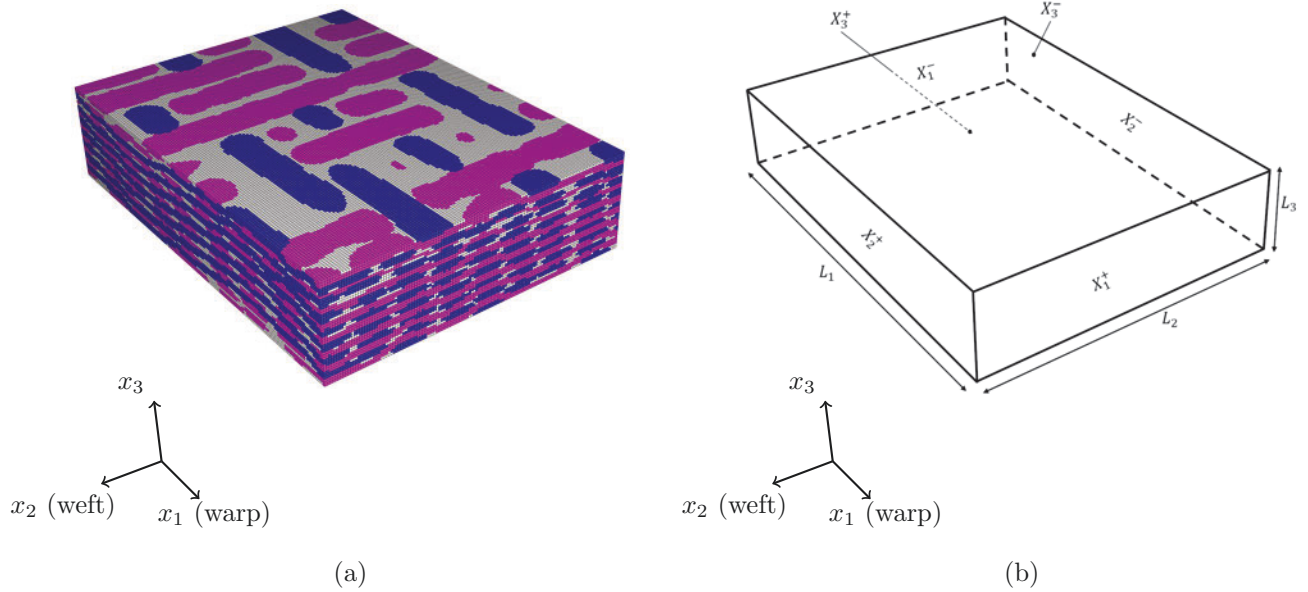

(a)

(b)

Figure B1: Example of the RVE at the meso-scale: (a) FEM model with 982 800 linear 8-node brick elements; (b) general geometry (L_i the unit cell edges lengths) with adopted classifications that are used for implementation of MUBC

Table B1: Mixed boundary conditions applied on the unit cell for the meso-scale homogenization. u_i denote displacements and L_i the unit cell edges lengths. For more details on notation refer to Figure B1(b)

Load-case	X_1^-	X_1^+	X_2^-	X_2^+	X_3^-	X_3^+
Tensile 1	$u_1 = 0$	$u_1 = L_1$	$u_2 = 0$	$u_2 = 0$	$u_3 = 0$	$u_3 = 0$
Tensile 2	$u_1 = 0$	$u_1 = 0$	$u_2 = 0$	$u_2 = L_2$	$u_3 = 0$	$u_3 = 0$
Tensile 3	$u_1 = 0$	$u_1 = 0$	$u_2 = 0$	$u_2 = 0$	$u_3 = 0$	$u_3 = L_3$
Shear 12	$u_2 = -L_1/4$ $u_3 = 0$	$u_2 = L_1/4$ $u_3 = 0$	$u_1 = -L_2/4$ $u_3 = 0$	$u_1 = L_2/4$ $u_3 = 0$	$u_3 = 0$	$u_3 = 0$
Shear 23	$u_1 = 0$	$u_1 = 0$	$u_3 = -L_2/4$ $u_1 = 0$	$u_3 = L_2/4$ $u_1 = 0$	$u_2 = -L_3/4$ $u_1 = 0$	$u_2 = L_3/4$ $u_1 = 0$
Shear 31	$u_3 = -L_1/4$ $u_2 = 0$	$u_3 = L_1/4$ $u_2 = 0$	$u_2 = 0$	$u_2 = 0$	$u_1 = -L_3/4$ $u_2 = 0$	$u_1 = L_3/$ $u_2 = 0$

References

[1] D. J. Michaud, A. N. Beris, P. S. Dhurjati, Curing behavior of thick-sectioned RTM composites, Journal of Composite Materials 32 (14) (1998) 1273–1296. doi:10.1177/002199839803201402.

[2] T. J. Corden, I. A. Jones, D. T. Jones, V. Middleton, The mechanisms of interlaminar cracking in thick resin transfer moulded composite cylinders, Composites Part A: Applied Science and Manufacturing 29 (4) (1998) 455–464. doi:10.1016/S1359-835X(97)00083-3.

[3] E. Ruiz, F. Trochu, Numerical analysis of cure temperature and internal stresses in thin and thick RTM parts, Composites Part A: Applied Science and Manufacturing 36 (6) (2005) 806–826. doi:10.1016/j.compositesa.2004.10.021.

[4] K. S. Kim, H. T. Hahn, Residual stress development during processing of graphite/epoxy composites, Composites Science and Technology 36 (2) (1989) 121–132. doi:10.1016/0266-3538(89)90083-3.

[5] D. Radford, R. Diefendorf, Shape Instabilities in Composites Resulting from Laminate Anisotropy, Journal of Reinforced Plastics and Composites 12 (1) (1993) 58–75. doi:10.1177/073168449301200104.

[6] D. W. Radford, T. S. Rennick, Separating sources of manufacturing distortion in laminated composites, Journal of Reinforced Plastics and Composites 19 (8) (2000) 621–641. doi:10.1106/CRMP-ARE5-GVPP-0Y7N.

[7] M. R. Wisnom, M. Gigliotti, N. Ersoy, M. Campbell, K. D. Potter, No Title, Composites Part A: Applied Science and Manufacturing 37 (4) (2006) 522–529.

[8] S. White, H. Hahn, Cure Cycle Optimization for the Reduction of Processing-Induced Residual Stresses in Composite Materials, Journal of Composite Materials 27 (14) (1993) 1352–1378. doi:10.1177/002199839302701402.

[9] N. Ersoy, M. Tugutlu, Cure kinetics modeling and cure shrinkage behavior of a thermosetting composite, Polymer Engineering & Science 50 (1) (2010) 84–92. doi:10.1002/pen.21514.

[10] P. Boisse, Advances in Composites Manufacturing and Process Design, Elsevier, 2015. doi:10.1016/C2014-0-02644-5.

[11] V. V. Vasiliev, E. Morozov, Advanced Mechanics of Composite Materials., Elsevier, 2007.

[12] C. Bellini, L. Sorrentino, Analysis of cure induced deformation of CFRP U-shaped laminates, Composite Structures 197 (2018) 1–9. doi:10.1016/j.compstruct.2018.05.038.

[13] A. A. Johnston, An integrated model of the development of process-induced deformation in autoclave processing of composite, Ph.D. thesis, The University of British Columbia (1997). doi:10.14288/1.0088805.

[14] L. Khoun, R. De Oliveira, V. Michaud, P. Hubert, Investigation of process-induced strains development by fibre Bragg grating sensors in resin transfer moulded composites, Composites Part A: Applied Science and Manufacturing 42 (3) (2011) 274–282. doi:10.1016/j.compositesa.2010.11.013.

[15] C. Wang, L. Yin, L. Zhang, D. Xiang, R. Gao, Metal Oxide Gas Sensors: Sensitivity and Influencing Factors, Sensors 10 (3) (2010) 2088–2106. doi:10.3390/s100302088.

[16] A. Courtois, M. Hirsekorn, M. Benavente, A. Jaillon, L. Marcin, E. Ruiz, M. Lévesque, Viscoelastic behavior of an epoxy resin during cure below the glass transition temperature: Characterization and modeling, Journal of Composite Materials 53 (2) (2018) 155–171. doi:10.1177/0021998318781226.

[17] A. Courtois, L. Marcin, M. Benavente, E. Ruiz, M. Lévesque, Numerical multiscale homogenization approach for linearly viscoelastic 3D interlock woven composites, International Journal of Solids and Structures 163 (2019) 61–74. doi:10.1016/j.ijsolstr.2018.12.018.

[18] A. Ding, S. Li, J. Sun, J. Wang, L. Zu, A thermo-viscoelastic model of process-induced residual stresses in composite structures with considering thermal dependence, Composite Structures 136 (2016) 34–43.

[19] M. Benavente, L. Marcin, A. Courtois, M. Lévesque, E. Ruiz, Viscoelastic distortion in asymmetric plates during post curing, Composites Part A: Applied Science and Manufacturing 103 (2017) 122–130. doi:10.1016/j.compositesa.2017.09.017.

[20] M. Benavente, L. Marcin, A. Courtois, M. Lévesque, E. Ruiz, Numerical analysis of viscoelastic process-induced residual distortions during manufacturing and post-curing, Composites Part A: Applied Science and Manufacturing 107 (2018) 205–216. doi:10.1016/j.compositesa.2018.01.005.

[21] A. A. Gusev, Representative volume element size for elastic composites: A numerical study, Journal of the Mechanics and Physics of Solids 45 (9) (1997) 1449–1459. doi:10.1016/S0022-5096(97)00016-1.

[22] J. Segurado, J. Llorca, A numerical approximation to the elastic properties of sphere-reinforced composites, Journal of the Mechanics and Physics of Solids 50 (10) (2002) 2107–2121. doi:10.1016/S0022-5096(02)00021-2.

[23] C. González, J. LLorca, Mechanical behavior of unidirectional fiber-reinforced polymers under transverse compression: Microscopic mechanisms and modeling, Composites Science and Technology 67 (13) (2007) 2795–2806. doi:10.1016/j.compscitech.2007.02.001.

[24] F. Fisher, L. Brinson, Viscoelastic interphases in polymer–matrix composites: theoretical models and finite-element analysis, Composites Science and Technology 61 (5) (2001) 731–748. doi:10.1016/S0266-3538(01)00002-1.

[25] M. Lévesque, K. Derrien, L. Mishnaevski, D. Baptiste, M. D. Gilchrist, A micromechanical model for nonlinear viscoelastic particle reinforced polymeric composite materials—undamaged state, Composites Part A: Applied Science and Manufacturing 35 (7-8) (2004) 905–913. doi:10.1016/J.COMPOSITESA.2004.02.017.

[26] A. H. Muliana, J. S. Kim, A concurrent micromechanical model for predicting nonlinear viscoelastic responses of composites reinforced with solid spherical particles, International Journal of Solids and Structures 44 (21) (2007) 6891–6913. doi:10.1016/J.IJSOLSTR.2007.03.016.

[27] A. H. Muliana, R. Haj-Ali, A multi-scale framework for layered composites with thermo-rheologically complex behaviors, International Journal of Solids and Structures 45 (10) (2008) 2937–2963. doi:10.1016/J.IJSOLSTR.2008.01.015.

[28] S. Sawant, A. Muliana, A thermo-mechanical viscoelastic analysis of orthotropic materials, Composite Structures 83 (1) (2008) 61–72. doi:10.1016/J.COMPSTRUCT.2007.03.008.

[29] N. Zobeiry, S. Malek, R. Vaziri, A. Poursartip, A differential approach to finite element modelling of isotropic and transversely isotropic viscoelastic materials, Mechanics of Materials 97 (2016) 76–91. doi:10.1016/J.MECHMAT.2016.02.013.

[30] M. Benavente, Viscoelastic distortion during manufacturing and post-curing of thermoset composites: Characterization and modeling, Ph.D. thesis, Polytechnique Montreal (2017).

[31] B. Widom, Random Sequential Addition of Hard Spheres to a Volume, The Journal of Chemical Physics 44 (10) (1966) 3888. doi:10.1063/1.1726548.

[32] J. L. Finney, Fine structure in randomly packed, dense clusters of hard spheres, Materials Science and Engineering 23 (2-3) (1976) 199–205. doi:10.1016/0025-5416(76)90194-4.

[33] D. He, N. Ekere, L. Cai, Computer simulation of random packing of unequal particles, Physical Review E 60 (6) (1999) 7098–7104. doi:10.1103/PhysRevE.60.7098.

[34] B. Drach, I. Tsukrov, A. Trofimov, Comparison of full field and single pore approaches to homogenization of linearly elastic materials with pores of regular and irregular shapes, International Journal of Solids and Structures 96 (2016) 48–63. doi:10.1016/j.ijsolstr.2016.06.023.

[35] F. Stig, S. Hallström, Spatial modelling of 3D-woven textiles, Composite Structures 94 (5) (2012) 1495–1502. doi:10.1016/J.COMPSTRUCT.2011.12.003.

[36] Z. Yang, W. Ren, R. Sharma, S. McDonald, M. Mostafavi, Y. Vertyagina, T. Marrow, In-situ X-ray computed tomography characterisation of 3D fracture evolution and image-based numerical homogenisation of concrete, Cement and Concrete Composites 75 (2017) 74–83. doi:10.1016/j.cemconcomp.2016.10.001.

[37] A. Trofimov, T. Mishurova, L. Lanzoni, E. Radi, G. Bruno, I. Sevostianov, Microstructural analysis and mechanical properties of concrete reinforced with polymer short fibers, International Journal of Engineering Science 133 (2018) 210–218. doi:10.1016/J.IJENGSCI.2018.09.009.

[38] A. C. Loos, G. S. Springer, Curing of Epoxy Matrix Composites, Journal of Composite Materials 17 (2) (1983) 135–169. doi:10.1177/002199838301700204.

[39] J. M. Svanberg, J. A. Holmberg, Prediction of shape distortions Part I. FE-implementation of a path dependent constitutive model, Composites Part A: Applied Science and Manufacturing 35 (6) (2004) 711–721. doi:10.1016/j.compositesa.2004.02.005.

[40] E. Ruiz, F. Trochu, Thermomechanical Properties during Cure of Glass-Polyester RTM Composites: Elastic and Viscoelastic Modeling, Journal of Composite Materials 39 (10) (2005) 881–916. doi:10.1177/0021998305048732.

[41] M. A. Biot, Theory of stress-strain relations in anisotropic viscoelasticity and relaxation phenomena, Journal of Applied Physics 25 (11) (1954) 1385–1391. doi:10.1063/1.1721573.

[42] R. A. Schapery, Application of thermodynamics to thermomechanical, fracture, and birefringent phenomena in viscoelastic media, Journal of Applied Physics 35 (5) (1964) 1451–1465. doi:10.1063/1.1713649.

[43] M. Lévesque, K. Derrien, D. Baptiste, M. D. Gilchrist, On the development and parameter identification of Schapery-type constitutive theories, Mechanics of Time-Dependent Materials 12 (2) (2008) 95–127. doi:10.1007/s11043-008-9052-y.

[44] G. P. Styan, Hadamard products and multivariate statistical analysis, Linear Algebra and its Applications 6 (1973) 217–240. doi:10.1016/0024-3795(73)90023-2.

[45] T. Crochon, Modeling of the viscoelastic behavior of a polyimide matrix at elevated temperature, Ph.D. thesis, PolytechniqueMontréal (2014).

[46] O. C. Zienkiewicz, M. Watson, I. P. King, A numerical method of visco-elastic stress analysis, International Journal of Mechanical Sciences 10 (10) (1968) 807–827. doi:10.1016/0020-7403(68)90022-2.

[47] J. C. Lagarias, J. A. Reeds, M. H. Wright, P. E. Wright, Convergence Properties of the Nelder–Mead Simplex Method in Low Dimensions, SIAM Journal on Optimization 9 (1) (1998) 112–147. doi:10.1137/S1052623496303470.

[48] T. A. Bogetti, J. W. Gillespie, Process-Induced Stress and Deformation in Thick-Section Thermoset Composite Laminates, Journal of Composite Materials 26 (5) (1992) 626–660. doi:10.1177/002199839202600502.

[49] P. A. Olivier, A note upon the development of residual curing strains in carbon/epoxy laminates. Study by thermomechanical analysis, Composites Part A: Applied Science and Manufacturing 37 (4) (2006) 602–616. doi:10.1016/j.compositesa.2005.05.006.

[50] M. Péron, R. Cardinaud, N. Lefèvre, J. Aubril, V. Sobotka, N. Boyard, S. Le Corre, PvT-HADDOC: A multi-axial strain analyzer and cure monitoring device for thermoset composites characterization during manufacturing, Composites Part A: Applied Science and Manufacturing 101 (2017) 129–142. doi:10.1016/j.compositesa.2017.06.004.
URL http://dx.doi.org/10.1016/j.compositesa.2017.06.004 https://linkinghub.elsevier.com/retrieve/pii/S1359835X17302336

[51] O. Pierard, C. Friebel, I. Doghri, Mean-field homogenization of multi-phase thermo-elastic composites: a general framework and its validation, Composites Science and Technology 64 (10-11) (2004) 1587–1603. doi:10.1016/j.compscitech.2003.11.009.

[52] K. A. Khan, A. H. Muliana, Effective thermal properties of viscoelastic composites having field-dependent constituent properties, Acta Mech 209 (2010) 153–178. doi:10.1007/s00707-009-0171-6.

[53] S. V. Lomov, D. S. Ivanov, I. Verpoest, M. Zako, T. Kurashiki, H. Nakai, S. Hirosawa, Meso-FE modelling of textile composites: Road map, data flow and algorithms, Composites Science and Technology 67 (9) (2007) 1870–1891. doi:10.1016/j.compscitech.2006.10.017.

[54] J. Skoček, J. Zeman, M. Šejnoha, Effective properties of textile composites: application of the Mori–Tanaka method, Modelling and Simulation in Materials Science and Engineering 16 (8) (2008) 085002. doi:10.1088/0965-0393/16/8/085002.

[55] S. Le Digabel, Algorithm 909: NOMAD: Nonlinear Optimization with the MADS Algorithm, ACM Transactions on Mathematical Software 37 (4) (2011) 1–15. doi:10.1145/1916461.1916468.

[56] I. Verpoest, S. V. Lomov, Virtual textile composites software WiseTex: Integration with micro-mechanical, permeability and structural analysis, Composites Science and Technology 65 (15-16 SPEC. ISS.) (2005) 2563–2574. doi:10.1016/j.compscitech.2005.05.031.

[57] D. H. Pahr, H. J. Böhm, Assessment of mixed uniform boundary conditions for predicting the mechanical behavior of elastic and inelastic discontinuously reinforced composites, CMES - Computer Modeling in Engineering and Sciences 34 (2) (2008) 117–136. doi:10.3970/cmes.2008.034.117.

[58] Y. Benveniste, A new approach to the application of Mori-Tanaka's theory in composite materials, Mechanics of Materials 6 (2) (1987) 147–157. doi:10.1016/0167-6636(87)90005-6.

[59] M. Kachanov, I. Tsukrov, B. Shafiro, Effective Moduli of Solids With Cavities of Various Shapes, Applied Mechanics Reviews 47 (1S) (1994) S151. doi:10.1115/1.3122810.

[60] I. Sevostianov, On the thermal expansion of composite materials and cross-property connection between thermal expansion and thermal conductivity, Mechanics of Materials 45 (2012) 20–33. doi:10.1016/j.mechmat.2011.10.001.

[61] I. Sevostianov, M. Kachanov, Explicit elasticity–conductivity connections for composites with anisotropic inhomogeneities, Journal of the Mechanics and Physics of Solids 55 (10) (2007) 2181–2205. doi:10.1016/j.jmps.2007.03.014.